

Role of FLR effects in magnetopause equilibrium

G. Ballerini^{† 1,2} and L. Rezeau¹ and G. Belmont¹ and F. Califano²

¹LPP, CNRS/Sorbonne Université/Université Paris-Saclay/Observatoire de Paris/Ecole Polytechnique,
Institut Polytechnique de Paris, Paris, France

²Dipartimento di Fisica E. Fermi, University of Pisa, Italy

(Received xx; revised xx; accepted xx)

The Earth magnetopause, when sufficiently plane and stationary at a local scale, can be considered as a "quasi-tangential" discontinuity, since the normal component of the magnetic field B_n is typically very small but not zero. Contrary to observations, the "Classic Theory of Discontinuities" (CTD) predicts that rotational and compressional jumps should be mutually exclusive in the general case $B_n \neq 0$, but allows only one exception: the tangential discontinuity provided that B_n is strictly zero. Here we show that Finite Larmor Radius (FLR) effects play an important role in the quasi-tangential case, whenever the ion Larmor radius is not fully negligible with respect to the magnetopause thickness. By including FLR effects, the results suggest that a rotational discontinuity undergoes a change comparable to the change of a Shear Alfvén into a Kinetic Alfvén wave when considering linear modes. For this new kind of discontinuity, the co-existence of rotational and compressional variations at the magnetopause does no more imply that this boundary is a strict tangential discontinuity, even in 1D-like regions far from X-lines if any. This result may lead to important consequences concerning the oldest and most basic questions of magnetospheric physics: how can the magnetopause be open, where and when? The role of FLR being established theoretically, the paper then shows that it can be proved experimentally. For that, we make use of MMS data and process them with the most recent available 4 spacecraft tools. First, we present the different processing techniques that we use to estimate spatial derivatives, such as $grad(B)$ and $div(P)$, and the magnetopause normal direction. We point out why this normal direction must be determined with extremely high accuracy to make the conclusions unambiguous. Then, the results obtained by these techniques are presented in a detailed case study and on a statistical basis.

Introduction

In space physics, there is a natural tendency of the medium to self-organize into distinct cells, separated by thin layers. This behavior can be observed at very different scales. Notable examples are planetary magnetospheres, which are bubbles in the solar wind stream and which are separated from it by bow shocks and magnetopauses (Parks 2019; Kivelson & Russell 1995; Belmont *et al.* 2014). The interaction of the solar wind with unmagnetized bodies such as comets also produces similar bubbles (Coates 1997; Bertucci 2005). The Solar System itself is a bubble in the flow of the local interstellar cloud, and it is separated from it by the heliopause and at least one shock ("termination shock") (Lallement 2001; Richardson *et al.* 2022). Similar cells and thin layers can also form spontaneously, far from any boundary condition as in the context of a turbulent medium (Frisch 1995; Chasapis *et al.* 2015).

Among all these thin layers, the terrestrial magnetopause plays a particular role. This region has been explored by a large number of spacecraft since the beginning of the space era, up to the most recent multi-spacecraft missions as Cluster (Escoubet *et al.* 1997, 2001) and MMS (Burch & Phan 2016), allowing for a detailed description of its properties. In addition, due to a very small

[†] Email address for correspondence: giulio.ballerini@lpp.polytechnique.fr

43 normal component of the magnetic field with respect to the magnetopause (defined $B_n = \mathbf{B} \cdot \mathbf{n}$
 44 where \mathbf{B} is the magnetic field and \mathbf{n} the magnetopause's normal) it can be identified as a "quasi-
 45 tangential" layer. This feature is a direct consequence of the frozen-in property that prevails at
 46 large scales, on both sides of the boundary, almost preventing any penetration of magnetic flux
 47 and matter between the solar wind and the magnetospheric media (both of them being magnetised
 48 plasmas). By large scales here we refer to the fluid scales where an ideal Ohm's law holds,
 49 as in the ideal magnetohydrodynamic (MHD) regime. However, small departures from a strict
 50 separation between the two plasmas do exist, at least locally and for a given time interval, and
 51 they are known to have important consequences for all the magnetospheric dynamics: substorms,
 52 auroras, etc (McPherron 1979; Tsurutani *et al.* 2001).

53 Knowing when and where plasma injection occurs through the magnetopause has been
 54 one of the hottest subjects of research since decades (Haaland *et al.* (2021) and references
 55 therein, Lundin & Dubinin (1984); Gunell *et al.* (2012); Paschmann *et al.* (2018a)). The largest
 56 consensus presently considers the equilibrium state of the boundary, valid on the major part
 57 of its surface, as a tangential discontinuity, with a strictly null B_n , while plasma injection is
 58 allowed only around a few reconnection regions, where the gradients characterizing the layer
 59 present 2D features. For that purpose, many studies have been carried out to understand where
 60 magnetic reconnection occurs the most (Fuselier *et al.* 2011; Trattner *et al.* 2021). Moreover,
 61 the conditions under which the magnetopause opens due to magnetic reconnection has been
 62 studied theoretically (Swisdak *et al.* 2003) and experimentally (Gosling *et al.* 1982; Paschmann
 63 1984; Phan *et al.* 2000; Fuselier *et al.* 2011; Vines *et al.* 2015). The results of the present study
 64 may allow reconsidering this paradigm by questioning the necessity of a strictly tangential
 65 discontinuity for the basic equilibrium state.

66
 67 In the whole paper hereafter, we will call one-dimensional all geometries in which the gradients
 68 of all parameters are in the same direction \mathbf{N} . In this sense, a plane magnetopause with not
 69 tangential gradient is said here to be 1D, while it would be considered 2D if considering real
 70 space instead of k space.

71 1. Classic Theory of Discontinuities

72 At every layer, the downstream and upstream physical quantities are linked by the fundamental
 73 conservation laws: mass, momentum, energy and magnetic flux (Landau & Lifshitz 1987). The
 74 simplest case occurs whenever the number of conservation laws is equal to the number of
 75 parameters characterizing the plasma state. When this condition is met, the possible downstream
 76 states are uniquely determined as a function of the upstream state, regardless of the (non-ideal)
 77 physics at play within the layer. In particular, it is possible to describe pressure variations without
 78 any closure equation. In this case, the jumps of all quantities are determined by a single scalar
 79 parameter (namely the "shock parameter" in neutral gas).

80 We refer hereafter to the "Classic Theory of Discontinuities" (CTD) as for the theory
 81 corresponding to this condition, which is used both for neutral media and (magnetized) plasmas.
 82 CTD is characterized by the following simplifying assumptions: a stationary layer, 1D variations,
 83 and isotropic pressure on both sides. For plasmas, the additional assumption of an ideal Ohm's
 84 law on both sides is considered (Belmont *et al.* 2019).

85 In CTD the conservation laws provide a system of jump equations between the upstream and
 86 downstream physical quantities, namely the Rankine-Hugoniot conditions in neutral media and
 87 generalized Rankine-Hugoniot conditions in plasmas.

88 The sets of equations used to compute the linear modes in hydrodynamics (HD) and MHD are
 89 similar to these jump equations system. simply because the HD and MHD models rely on the
 90 same conservation laws as Rankine-Hugoniot and generalized Rankine-Hugoniot respectively

91 A direct consequence is that many properties are shared by the solutions of the two types of
 92 systems: linear modes and discontinuities. For a neutral medium, the linear sound wave solution
 93 corresponds to the well-known sonic shock solution, while for a magnetized plasma, the two
 94 magnetosonic waves correspond to the two main types of MHD shocks: fast and slow. However,
 95 an additional discontinuity solution, the intermediate shock, has no linear counterpart. The
 96 intermediate shock presents a reversal of the tangential magnetic field through the discontinuity,
 97 which is not observed neither in the fast nor in the slow mode. Furthermore, a non-compressional
 98 solution exists in both types of systems, represented by the shear Alfvén mode for linear MHD,
 99 and by the "rotational discontinuity" solution for the generalized Rankine-Hugoniot system.

100 Focusing on magnetized plasma physics, CTD leads to distinguish compressive and rotational
 101 discontinuities. An important feature of these solutions is that the compressional and rotational
 102 solutions are mutually exclusive: the shock solutions are purely compressional, without any
 103 rotation of the tangential magnetic field (this is called the "coplanarity property"), while the
 104 rotational discontinuity does imply such a rotation but without any variation of the magnetic field
 105 amplitude and without any compression of the particle density (Fig.1). This distinction persists
 106 whatever the fluxes along the discontinuity normal, even when the normal components u_n and B_n
 107 of the velocity and the magnetic field are arbitrarily small. The only exception is the "tangential
 108 discontinuity" when both normal fluxes are strictly zero. This solution would correspond, for the
 109 magnetopause, to the case without any connection between solar wind and magnetosphere. It
 110 appears as a singular case since the tangential discontinuity, with $B_n = 0$, is not the limit of any
 111 of the general solutions with $B_n \neq 0$. While the limit always implies two solutions, one purely
 112 rotational and the other purely compressional, the singular solution $B_n = 0$ only provides one
 113 solution where the two characters can coexist.

114 In the solar wind, discontinuities are routinely observed and several authors have performed
 115 statistics for a long time to determine the proportion of the different kinds of discontinuities,
 116 mainly focusing on the tangential and rotational ones. They conclude that in most cases
 117 tangential discontinuities (*i.e.* with B_n small enough to be barely measurable) are the most
 118 ubiquitous (see Colburn & Sonett (1966), for a pioneering work in this domain and Neugebauer
 119 (2006); Paschmann *et al.* (2013); Liu *et al.* (2022), and references therein, for more recent
 120 contributions). In these studies, rotational discontinuities are identified only when B_n is large
 121 enough. However, many discontinuities present features that are typical of both rotational and
 122 tangential discontinuities and are classified as "either" of the two. Extending these studies in the
 123 range of small B_n , where all discontinuities are not necessarily "tangential discontinuities" in the
 124 CTD sense, requires the study of the quasi-tangential case.

125 2. The Earth's magnetopause

126 Thanks to *in-situ* observations, the Earth's magnetopause has a pivotal role in testing the
 127 discontinuity theories. Indeed, the Earth's magnetopause boundary exhibits, over its entire
 128 surface, both a rotation of the magnetic field (Sonnerup & Ledley 1974) and a density
 129 variation (Otto 2005) since it is the junction of two media, the magnetosheath and the
 130 magnetosphere where the magnetic field and the density are different (Dorville *et al.* 2014).

131 As stated above, the usual paradigm is that the magnetopause is always a tangential
 132 discontinuity and that it becomes "opens" only exceptionally at a few points where the
 133 boundary departs from one-dimensionality due to magnetic reconnection. Does it mean that it
 134 justifies the very radical hypothesis of a magnetopause nearly completely impermeable to mass
 135 and magnetic flux, with strictly null B_n and u_n and quasi-independent plasmas on both sides
 136 (apart from the normal pressure equilibrium)? From a theoretical point of view, it is clear that the
 137 singular limit from $B_n \simeq 0$ to $B_n = 0$ remains to be solved. From an experimental point of view,
 138 if the components B_n and u_n are known to be always very small, the observations can hardly

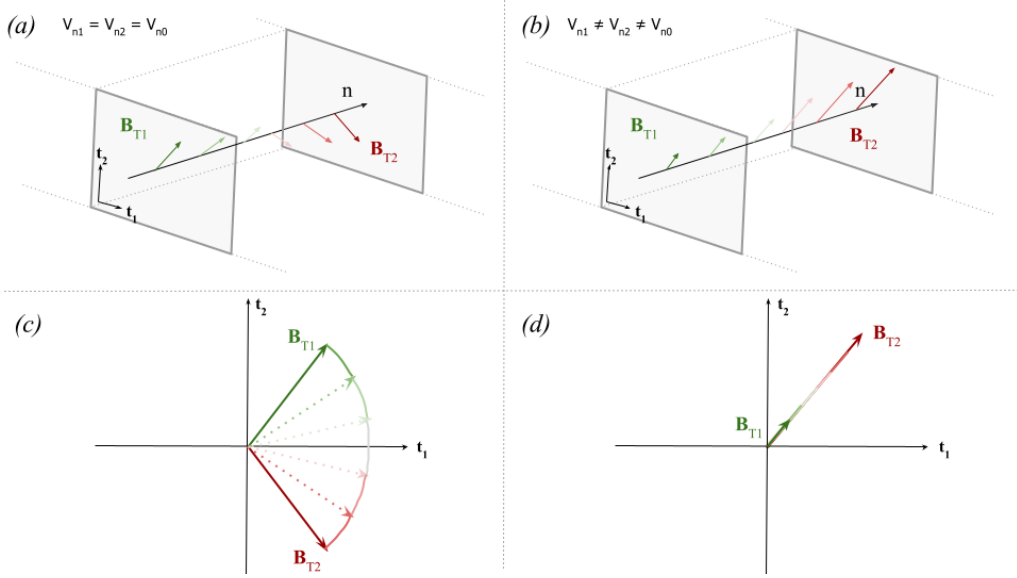


FIGURE 1. Cartoon showing the different variations of B between a rotational discontinuity (left) and a compressive one (right). The top panel shows in 3D the variation of B inside the magnetopause plane; the bottom panel shows the hodogram in this tangential plane: a circular arc for the rotational discontinuity and a radial line for shocks.

139 distinguish between $B_n \simeq 0$ and $B_n = 0$ because of the uncertainties, due to the fluctuations and
 140 the limited accuracy in determining the normal direction (Rezeau *et al.* 2018; Haaland *et al.*
 141 2004; Dorville *et al.* 2015b).

142 The results of the present paper will question the above paradigm. We will show theoretically
 143 and experimentally that CTD fails at the magnetopause and that rotation and compression can
 144 actually coexist with finite B_n and u_n , even in the 1D case. Such a paradigm change may be
 145 reminiscent of a similar improvement in the theoretical modeling of the magnetotail in the 70's
 146 studies (Coppi *et al.* (1966); Galeev (1979); Coroniti (1980) and references therein). In that case
 147 the authors demonstrated that even a very weak component of the magnetic field across the
 148 current layer was sufficient to completely modify the stability properties of the plasmashet, so
 149 that the finite value of B_n had to be taken into account, contrary to the pioneer versions of the
 150 tearing instability theories.

151 3. The role of pressure

152 In CTD the separation between the compressional and rotational properties of the
 153 discontinuities comes from only two equations projected on the tangential plane. These
 154 equations are the momentum equation and the Faraday - Ohm's law, that read:

$$155 \rho \frac{d\mathbf{u}}{dt} + \nabla \cdot \mathbf{P}_i + \nabla \cdot \mathbf{P}_e = \mathbf{J} \times \mathbf{B} \quad (3.1)$$

$$156 \nabla \times \mathbf{E} = -\frac{\partial \mathbf{B}}{\partial t}$$

$$157 \text{ where } \mathbf{E} = -\mathbf{u} \times \mathbf{B} + \frac{1}{ne} \mathbf{J} \times \mathbf{B} - \frac{1}{ne} \nabla \cdot \mathbf{P}_e \quad (3.2)$$

158 where \mathbf{B} is the magnetic field and \mathbf{u} is the flow velocity in a reference frame where the layer is
 steady.

159 Considering one-dimensional gradients along the normal direction \mathbf{n} , neglecting the non-ideal
 160 terms in Ohm's law and integrating across the layer, these two equations, projected on the
 161 tangential plane, give:

$$162 \quad \rho_2 u_{n2} \mathbf{u}_{t2} - B_{n2} \mathbf{B}_{t2} / \mu_0 = \rho_1 u_{n1} \mathbf{u}_{t1} - B_{n1} \mathbf{B}_{t1} / \mu_0 \quad (3.3)$$

$$163 \quad B_{n2} \mathbf{u}_{t2} - u_{n2} \mathbf{B}_{t2} = B_{n1} \mathbf{u}_{t1} - u_{n1} \mathbf{B}_{t1} \quad (3.4)$$

164 Due to the divergence free equation, the values B_{n1} and B_{n2} are equal and will be written as
 165 B_n without index in the following. Similarly, $\rho_1 u_{n1}$ and $\rho_2 u_{n2}$ are equal because of the continuity
 166 equation and will be simply noted ρu_n in the following. Here, the indices n and t indicate the
 167 projection along the normal and in the tangential plane, respectively, while indices 1 and 2
 168 indicate the two sides of the discontinuity. It is important to note that, in CTD, the pressure
 169 divergence terms do not appear in Eq.(3.3) because of the assumption done in this theory that the
 170 pressure is isotropic on both sides so that their integration gives terms of the form $(p_2 - p_1)\mathbf{n}$,
 with no component in the tangential plane.

171 We see that all terms in these two equations are proportional to B_n or u_n , so that any non-
 172 ideal term, even small, can become dominant when these two quantities tend to zero (if these
 173 non-ideal terms do not tend to zero at the same time). As the distinction between compressional
 174 and rotational character fully relies on this system of equations, this evidences the necessity
 175 of investigating the quasi-tangential case for resolving the usual singularity of the tangential
 176 discontinuity. We note that the LHS and RHS of equation 3.4 can be put equal to zero by choosing
 177 the "De Hoffmann-Teller" tangential reference frame where the electric field is zero (Belmont
 178 *et al.* 2019). However, this choice, even if it can simplify some calculations, is not necessary
 179 here. Finally, the variables \mathbf{u}_t can be eliminated from the system by a simple linear combination
 180 of the two equations, leading to:

$$(u_{n2} - u_{n0})\mathbf{B}_{t2} = (u_{n1} - u_{n0})\mathbf{B}_{t1} \quad (3.5)$$

181 where

$$u_{n0} = \frac{B_n^2}{\mu_0 \rho u_n} = \text{cst} \quad (3.6)$$

182 Equation (3.5) leads to the distinction between shocks, where the tangential magnetic fields
 183 on both sides are collinear (but with different modules), and rotational discontinuities, where
 184 the terms inside the brackets must be equal to zero. Rotational discontinuities correspond to
 185 a propagation velocity equal to the normal Alfvén velocity, and imply $u_{n1} = u_{n2} = u_{n0}$, and
 186 therefore an absence of compression of the plasma.

187 As previously stated, the separation between the compressional and rotational characters
 188 mainly derives, in CTD, from the assumption of isotropic pressures on both sides, which prevents
 189 the pressure divergences to have tangential components. When the isotropic hypothesis is relaxed
 190 (Hudson 1971), the set of conservation equations is no longer sufficient to determine a unique
 191 downstream state for a given upstream one. As a consequence, the global result depends on the
 192 non-ideal processes occurring within the layer. In addition to anisotropy effects, Finite Larmor
 193 Radius (FLR) effects can be expected to break the gyrotropy of the pressure tensor around \mathbf{B}
 194 in the case of thin boundaries between different plasmas. This means that the main effect that
 195 explains departures from CTD comes from the tangential component of the divergence of the
 196 pressure tensor, which must be taken into account in the momentum equation. On the other hand,
 197 the non-ideal effects related to the generalized Ohm's law are negligible, at least in the examples
 198 shown in this paper. The possible types of discontinuities in an anisotropic plasma have been
 199 discussed in several papers long time ago (Lynn 1967; Abraham-Shrauner 1967; Chao 1970;
 200 Neubauer 1970), and the present paper improves the analysis in the light of the new experimental
 201 possibilities given by the MMS measurements.

202 When the dynamics drives the conditions for the pressure tensor to become anisotropic (and
 203 *a fortiori* in the non-gyrotropic case) the $\nabla \cdot \mathbf{P}$ term comes into play linking upstream and
 204 downstream quantities. Considering the "simple" anisotropic case, *i.e.* keeping the gyrotropy
 205 around \mathbf{B} , it has been shown (Hudson 1971) that the $\nabla \cdot \mathbf{P}$ term then just introduces a new
 206 coefficient:

$$\alpha = 1 - \frac{P_{\parallel} - P_{\perp}}{B^2/\mu_0} \quad (3.7)$$

207 This coefficient has been interpreted as a change in the Alfvén velocity $V_{An}^2 = \alpha V_{An}^2$, but it
 208 appears more basically as a change in Eq.(3.5):

$$(u_{n2} - \alpha_2 u_{n0})\mathbf{B}_{t2} = (u_{n1} - \alpha_1 u_{n0})\mathbf{B}_{t1} \quad (3.8)$$

209 This equation shows that, in this simple anisotropic case, coplanar solutions still exist (\mathbf{B}_{t2}
 210 and \mathbf{B}_{t1} are collinear), but that whenever α_2 is not equal to α_1 , the equivalent of the rotational
 211 discontinuity now implies compression:

$$u_{n2} \neq u_{n1} \quad \text{if} \quad \alpha_2 \neq \alpha_1 \quad (3.9)$$

212 Since $u_{n2} = \alpha_2 u_{n0}$ and $u_{n1} = \alpha_1 u_{n0}$. The variation of u_n explains why the modified rotational
 213 discontinuity can be "evolutionary" (Jeffrey & Taniuti 1964), the non linear steepening being
 214 counter-balanced at equilibrium by non-ideal effects for a thickness comparable with the
 215 characteristic scale of these effects.

216 There is actually no additional conservation equation available that would allow the jump of
 217 the anisotropy coefficient α to be determined. Consequently, there is no universal result that gives
 218 the downstream state as a function of the upstream one, regardless of the microscopic processes
 219 going on within the layer. This remains valid for the full anisotropic case, with non-gyrotropy. As
 220 soon as the ion Larmor radius ρ_i and the ion inertial length d_i are not fully negligible with respect
 221 to the characteristic scale L of the layer, kinetic effects, and in particular FLR effects, which make
 222 the pressure tensor non-gyrotropic, must be taken into account to describe self-consistently the
 223 internal processes. Then, the effect of the divergence of the pressure tensor is no longer reduced
 224 to adding a coefficient α since its tangential component is no longer collinear with \mathbf{B}_t . Such
 225 effect has been already reported and analyzed in the context of magnetic reconnection (Aunai
 226 *et al.* 2013, 2011) and in kinetic modeling of purely tangential layers (Belmont *et al.* 2012;
 227 Dorville *et al.* 2015a). It has been also investigated in the case of linear modes where they are
 228 responsible for the transition from shear Alfvén into Kinetic Alfvén Wave (Hasegawa & Uberoi
 229 1982; Belmont & Rezeau 1987; Cramer 2001). On the other hand, it has never been introduced
 230 in the context of quasi-tangential discontinuities.

231 If a simple anisotropy preserving gyrotropy around \mathbf{B} can be straight fully taken into account
 232 for modeling the pressure tensor and using it in fluid equations, introducing non-gyrotropy does
 233 not lead to a general and simple modeling for the pressure tensor. It would demand *a priori*
 234 a full kinetic description or, at least, some expansions assuming that these effects are small
 235 enough (see Braginskii (1965) for the pioneer work in this field and Passot & Sulem (2006) and
 236 references therein). Several papers have investigated the changes in rotational discontinuities
 237 when such non-ideal effects are introduced (Lyu & Kan 1989; Hau & Sonnerup 1991; Hau
 238 & Wang 2016). These theoretical papers used different analytical models based on different
 239 simplifying assumptions. Contrary to these papers, we will not use such kind of assumptions.
 240 Instead, we will just analyze the observed magnetic hodograms, and show that their shape is
 241 incompatible with a gyrotropic pressure.

242 4. The magnetopause normal

243 When studying the magnetopause with *in situ* measurements, the most basic geometric
 244 characteristic to be determined is the normal to its surface (which may vary during the crossing).
 245 An accurate determination of the magnetopause normal is actually a fundamental condition for
 246 determining reliable estimates of the normal components of both the magnetic and the mass
 247 fluxes. Moreover, having a good estimation of the normal direction is also necessary to determine
 248 the speed of the structure and its thickness. Quantitatively speaking, to determine the normal
 249 component of the magnetic field sufficiently well (assuming that $B_n/|\mathbf{B}| \sim 2\%$), an accuracy of
 250 the normal should be of the order of $\delta\theta < 1^\circ$. In the literature, a good accuracy of determination
 251 of the normal is considered to be of the order of 5% (Denton *et al.* 2018).

252 Beyond determining the normal direction, some "reconstruction methods" can be used to
 253 provide a more global view of the large scale structure around the spacecraft. Although these
 254 methods have proven to provide remarkable results (De Keyser 2008; Hasegawa *et al.* 2005;
 255 Denton *et al.* 2020) they will not be used here (the first two studies assume the Grad-Shafranov
 256 equations to be valid, implying stationary MHD, and are therefore not appropriate to investigate
 257 the non-MHD effects such as the FLR effects).

258 Over the years, several methods have been developed with the purpose to precisely determine
 259 the normal direction (see e.g. (Haaland *et al.* 2004; Shi *et al.* 2019)). The most common is
 260 the minimum variance (MVA) introduced with the first measurements of the magnetic field in
 261 space (Sonnerup & Cahill 1967; Sonnerup & Scheible 1998). This method, which requires single
 262 spacecraft measurements, provides a *global* normal, *i.e.* a single normal vector for each entire
 263 time series across the boundary. The tool is based on the assumption that the boundary is a
 264 perfectly one-dimensional and stationary layer crossing the spacecraft. Other notable examples
 265 are the Generic Residue Analysis (GRA) technique (Sonnerup *et al.* 2006), which consist in
 266 a generalisation of the MVA to other parameters than \mathbf{B} , and the BV method (Dorville *et al.*
 267 2014), which combines magnetic field and velocity data. Even though these methods can give
 268 an accurate normal determination (Dorville *et al.* 2015b), they provide, like MVA, a *global*
 269 normal and thus they cannot provide the necessary basis for investigating the variations of
 270 the magnetopause normal within the structure and test the possible departures from mono-
 271 dimensionality. Let us finally recall that waves and turbulence, which are always superimposed
 272 to the laminar magnetopause profiles, bring strong limitations in the normal direction accuracy
 273 for all methods, in particular these global ones.

274 In this context, multi-spacecraft missions have represented a fundamental step in increasing
 275 the accuracy of the normal determination, allowing to determinate the gradients of the measured
 276 fields. A notable example is the Minimum Directional Derivative (MDD, Shi *et al.* (2005))
 277 method. This tool generally uses the magnetic field data, but it must be kept in mind that it
 278 is not based on specific properties of this field. The MDD technique is a so-called "gradient
 279 based method" since the calculation of the normal is based on the experimental estimation of the
 280 dyadic tensor $\mathbf{G} = \nabla\mathbf{B}$. This tensor gradient can be obtained from multispacecraft measurements
 281 using the reciprocal vector method (Chanteur 1998). The MDD method consists in diagonalizing
 282 the matrix $\mathbf{L} = \mathbf{G} \cdot \mathbf{G}^T$, finding the normal direction as the eigenvector corresponding to
 283 the maximum eigenvalue. Moreover, the gradient matrix can also be used for estimating the
 284 dimensionality of the boundary from the ratio between the eigenvalues. A way of finding a
 285 quantitative determination of this dimensionality was proposed in Rezeau *et al.* (2018).

286 For the vector \mathbf{B} , the MDD method makes use only of the spatial derivatives $\partial_i\mathbf{B}$, which are
 287 accessible at each time step thanks to the 4-point measurements today available with multi-
 288 spacecraft space missions. In this sense, it is the opposite of the MVA method, which makes
 289 use only of the temporal variances of the \mathbf{B} components. It therefore allows for an instantaneous
 290 determination of the normal at any point inside the layer, while MVA can only provide a single

291 normal for a full crossing. In addition, contrary to MVA, MDD does not make any assumption
 292 about the geometry of the layer (1D variations or not), and about the physical properties of the
 293 vector used. Indeed, it can be applied to the magnetic field data but also to any other vector since
 294 the property $\nabla \cdot \mathbf{B} = 0$ is not used.

295 However, due to waves and turbulence, the magnetopause can present locally two-dimensional
 296 properties that are insignificant for the profiles we are looking for. For this reason, we will focus
 297 here on intervals where the magnetopause is mainly one-dimensional, discarding the crossings in
 298 which local 2D features are observed. The intervals considered as one-dimensional are those for
 299 which $\lambda_{max} \gg \lambda_{int}$. Here λ_{max} and λ_{int} are defined as the highest and the intermediate eigenvalues
 300 of the matrix \mathbf{G} . In this limit, the ordering between λ_{int} and λ_{min} (*i.e.* the smaller eigenvalue) is
 301 not relevant in defining the intervals. Specifically, we use the parameter, $D_1 = (\lambda_{max} - \lambda_{int})/\lambda_{max}$,
 302 which enables us to quantify this mono-dimensionality of the magnetopause as a function of
 303 time.

304 A more recent tool proposed to study the magnetopause is the hybrid method presented in
 305 Denton *et al.* (2016, 2018), in which the orientation of the magnetopause is obtained through a
 306 combination of the MDD and MVA methods, resulting in an improved accuracy of the normal
 307 direction.

308 The only limitation to the MDD accuracy comes from the uncertainty of the spatial derivatives
 309 that it uses. In particular, the local gradient matrix is calculated through the reciprocal vector
 310 technique (Chanteur 1998), which assumes linear variations between the spacecraft. Because
 311 small-scale waves and turbulence are always superimposed on the magnetopause profiles being
 312 searched for, this assumption cannot be well respected without some filtering. This filtering
 313 actually leads to introduce part of the temporal information on the variations, but it still allows
 314 keeping local information inside the layer whenever one filters only the scales sufficiently smaller
 315 than those associated to the full crossing duration. The quality of the filtering is therefore the
 316 biggest challenge to complete for getting accurate results. For instance, simple gaussian filters
 317 done independently on the four spacecraft would provide insufficient accuracy: this can be
 318 observed by the fact that, when doing it, the relation $\nabla \cdot \mathbf{B} = 0$ is violated in the result. In
 319 the following section, it is shown how the MDD method can be included in a fitting procedure
 320 of the four spacecraft simultaneously and where this relation can be imposed as a constraint. We
 321 also show that, when no constraint is added, this procedure justifies the use of MDD with data
 322 that are filtered independently.

323 5. A new tool

324 The tool we present here, namely GF2 (Gradient matrix Fitting), has been derived from the
 325 MDD method. The digit 2 indicates that in the version of the tool that we use here the data
 326 are fitted with a 2D model (it can be shown that fitting with a 1D model is mathematically
 327 equivalent to the standard MDD technique used with smoothed data). Differently from the
 328 original method, we assume that the structure under investigation can be fitted locally (*i.e.* in each
 329 of the small sliding window used along the global crossing), by a two-dimensional model. This
 330 does not imply that the magnetopause is assumed globally two-dimensional. As for MDD, the
 331 instantaneous gradient matrix \mathbf{G} is obtained from the data using the reciprocal vector's technique
 332 (Chanteur 1998). When performing the 2D fit in each sliding window, we then impose some
 333 physical constraints, which could be checked only *a posteriori* with the classic MDD method.

334 The model \mathbf{G}_{fit} is obtained as follows:

$$\mathbf{G}_{fit} = \mathbf{e}_0 \mathbf{B}'_{e0} + \mathbf{e}_1 \mathbf{B}'_{e1} \quad (5.1)$$

335 where we define \mathbf{e}_0 and \mathbf{e}_1 as two unit vectors in the plane perpendicular to the direction of
 336 invariance and \mathbf{B}'_{e0} and \mathbf{B}'_{e1} as the variation of the magnetic field along these two directions.

337 By performing the fit, we impose $\nabla \cdot \mathbf{B} = 0$ (as used in MVA but ignored in standard MDD). In
 338 the model, this can be written as:

$$\mathbf{e}_0 \cdot \mathbf{B}'_{e0} + \mathbf{e}_1 \cdot \mathbf{B}'_{e1} = 0 \quad (5.2)$$

339 In order to fit the experimental \mathbf{G} by the model \mathbf{G}_{fit} , the following quantity has to be minimised

$$\begin{aligned} D_2 &= \text{Tr}[(\mathbf{G}_{fit} - \mathbf{G}) \cdot (\mathbf{G}_{fit} - \mathbf{G})^T] \\ &= \mathbf{B}'_{e0}{}^2 - 2\mathbf{e}_0 \cdot \mathbf{G} \cdot \mathbf{B}'_{e0} + \mathbf{B}'_{e1}{}^2 - 2\mathbf{e}_1 \cdot \mathbf{G} \cdot \mathbf{B}'_{e1} + \text{Tr}(\mathbf{G}\mathbf{G}^T) \end{aligned} \quad (5.3)$$

340 We can disregard the last term, since it is independent of the fit parameters. To impose the
 341 physical constraints, we use Lagrange multipliers, minimizing:

$$\begin{aligned} D_2 &= \mathbf{B}'_{e0}{}^2 - 2\mathbf{e}_0 \cdot \mathbf{G} \cdot \mathbf{B}'_{e0} + \mathbf{B}'_{e1}{}^2 - 2\mathbf{e}_1 \cdot \mathbf{G} \cdot \mathbf{B}'_{e1} + 2\lambda(\mathbf{e}_0 \cdot \mathbf{B}'_{e0} + \mathbf{e}_1 \cdot \mathbf{B}'_{e1}) \\ &= \mathbf{B}'_{e0}{}^2 - 2\mathbf{e}_0 \cdot (\mathbf{G} - \lambda\mathbf{I}) \cdot \mathbf{B}'_{e0} + \mathbf{B}'_{e1}{}^2 - 2\mathbf{e}_1 \cdot (\mathbf{G} - \lambda\mathbf{I}) \cdot \mathbf{B}'_{e1} \end{aligned} \quad (5.4)$$

342 By assuming in the first approximation that the direction of invariance \mathbf{e}_2 is known, we can
 343 choose the two vectors \mathbf{e}_0 and \mathbf{e}_1 as an arbitrary orthonormal basis for the plane of variance. For
 344 performing the minimisation, we have just to impose equal to zero the derivatives with respect to
 345 \mathbf{B}'_{e0} , \mathbf{B}'_{e1} and λ , obtaining Equation 5.2 and:

$$\mathbf{B}'_{e0} = \mathbf{e}_0 \cdot (\mathbf{G} - \lambda\mathbf{I}) \quad (5.5)$$

346

$$\mathbf{B}'_{e1} = \mathbf{e}_1 \cdot (\mathbf{G} - \lambda\mathbf{I}) \quad (5.6)$$

347 By introducing these two equations in Equation 5.2 we obtain:

$$\lambda = \frac{G_{00} + G_{11}}{2}, \quad (5.7)$$

348 from which we get the values of \mathbf{B}'_{e0} and \mathbf{B}'_{e1} . At this point, the matrix \mathbf{G}_{fit} is fully determined. We
 349 can then look for its eigenvalues and eigenvectors, as in the standard MDD method, and get the
 350 normal \mathbf{n} and the tangential directions \mathbf{t}_1 (*i.e.* the one orthogonal to the direction of invariance)
 351 from this smooth fit.

352 The choice of the direction of invariance has actually no major influence on the determination
 353 of the normal direction, neither on the estimation of the 2D effects. For large 2D effects, one
 354 could choose the direction of minimum variance obtained by applying directly the standard MDD
 355 method to the data. Nevertheless, for almost 1D cases (the most common situation), the spatial
 356 derivatives in the tangential directions are generally much smaller than the noise, so this result
 357 is not reliable. We simply choose here the constant M direction given by MVA, which is often
 358 considered as the direction of the X line if interpreted in the context of 2D models of magnetic
 359 reconnection (*cf.* for instance Phan *et al.* (2013) for a typical use of this choice and Aunai *et al.*
 360 (2016); Liu *et al.* (2018); Denton *et al.* (2018) for discussions about it).

361 Finally, another useful by-product of the method can be obtained: comparing the spatial
 362 derivatives and the temporal ones and using a new fitting procedure, we can compute the two
 363 components of the velocity of the structure V_{n0} and V_{t1} with respect to the spacecraft. Only the
 364 motion along the invariant direction then remains unknown.

365

5.1. Normal from ions mass flux

366 This tool can be easily adapted to any other vector dataset by just changing the physical
 367 constraint. In particular, we chose to study the structure using the ion mass flux data. In this
 368 case we impose mass conservation $\nabla \cdot \mathbf{\Gamma}_i = -\partial_t n_i$ (with $\mathbf{\Gamma}_i = n_i \mathbf{u}_i$). Eq.5.2 now writes

$$\mathbf{e}_0 \cdot \mathbf{\Gamma}'_{e0} + \mathbf{e}_1 \cdot \mathbf{\Gamma}'_{e1} + \partial_t n_i = 0 \quad (5.8)$$

Therefore, when using the Lagrange multipliers, Eq.5.4 changes to:

$$\begin{aligned} D_2 &= \mathbf{I}'_{e0}{}^2 - 2\mathbf{e}_0 \cdot \mathbf{G} \cdot \mathbf{I}'_{e0} + \mathbf{I}'_{e1}{}^2 - 2\mathbf{e}_1 \cdot \mathbf{G} \cdot \mathbf{I}'_{e1} + 2\lambda(\mathbf{e}_0 \cdot \mathbf{I}'_{e0} + \mathbf{e}_1 \cdot \mathbf{I}'_{e1} + \partial_t n_i) \\ &= \mathbf{I}'_{e0}{}^2 - 2\mathbf{e}_0 \cdot (\mathbf{G} - \lambda \mathbf{I}) \cdot \mathbf{I}'_{e0} + \mathbf{I}'_{e1}{}^2 - 2\mathbf{e}_1 \cdot (\mathbf{G} - \lambda \mathbf{I}) \cdot \mathbf{I}'_{e1} + 2\lambda \partial_t n_i \end{aligned} \quad (5.9)$$

By using the same algorithm as above, the constraint can now be written as:

$$\lambda = \frac{G_{00} + G_{11} + \partial_t n_i}{2} \quad (5.10)$$

5.2. Dimensionality index

From this procedure, we can also derive another significant result: we can obtain an indicator of the importance of the 2D effects in the profiles, free of the parasitic noise effects. Specifically, we can estimate the variation of the magnetic field along the normal by projecting the \mathbf{G}_{fit} matrix along it $\text{var}_n = |\mathbf{G}_{fit} \cdot \mathbf{n}|$. Consequently, if we designate the variation along \mathbf{t}_1 as var_t , we can introduce a new dimensionality index:

$$\mathcal{D}_{GF2} = \frac{\text{var}_n - \text{var}_t}{\text{var}_n} \quad (5.11)$$

This index can usefully be compared with the instantaneous index $D_1 = (\lambda_{max} - \lambda_{int})/\lambda_{max}$ of Rezeau *et al.* (2018).

6. Expected accuracy and tests of the tool

In this section we test the accuracy of the GF2 tool. To accomplish this, we exploit a case crossing, which will be investigated in detail in the following section. The crossing considered comes from MMS data (Burch & Phan 2016), taking place at around 22:11 on 28th December 2015. For this study we use data from the FluxGate Magnetometers (FGM, Russell *et al.* (2016)), providing the magnetic field data, the Electric Double Probe (EDP, Lindqvist *et al.* (2016); Ergun *et al.* (2016)), for the electric field, and Dual Ions and Electrons Spectrometer instrument (DIS, DES, Pollock *et al.* (2016)), for plasma measurements. An overview of the event is shown in Fig. 2, where both the magnetic field and ion bulk velocity are given in Geocentric Solar Ecliptic (GSE) coordinates. For this event, the spacecraft are located in [7.6, -6.7, -0.8] R_E in GSE coordinates (where R_E is the Earth's radius).

The temporal interval in which we observe the shear in the magnetic field and the crossing in the particle structure is about 8 seconds, enough to allow for high resolution for both sets of measurements. The crossing is chosen by also analyzing the dimensionality of the magnetic field measurements averaged along the crossing. In particular, the dimensionality parameter defined in Eq. 5.11, denoted as \mathcal{D}_{GF2} , and the one introduced in Rezeau *et al.* (2018), denoted as D_1 , were considered. In this interval, indeed, we have $D_{1,mean} = 0.97 \pm 0.03$ while $\mathcal{D}_{GF2} = 0.89 \pm 0.06$, both highlighting that the crossing exhibits one-dimensional features throughout the time interval. We remind here that in burst mode, the frequency of magnetic field measurements is 132Hz while it is 6,67 Hz for ions. To conduct the following study, it is necessary to interpolate all measurements at the same times. We did it by testing two sampling frequencies: the magnetic field and the ion ones. The results obtained are consistent with the two methods. All figures shown in the paper are obtained with the sampling times of the MMS1 magnetic field. Furthermore, the crossing is observed quasi-simultaneously for the two quantities, with a large interval where the two kinds of results can be compared.

As a first test, we compare in Fig.3 the normals obtained by GF2 and those by the standard MDD technique (using data smoothed in a 0.31s time-window), for both the magnetic field and the ion data. For reference, we also compare the result of $GF2_B$ with the MVA one.

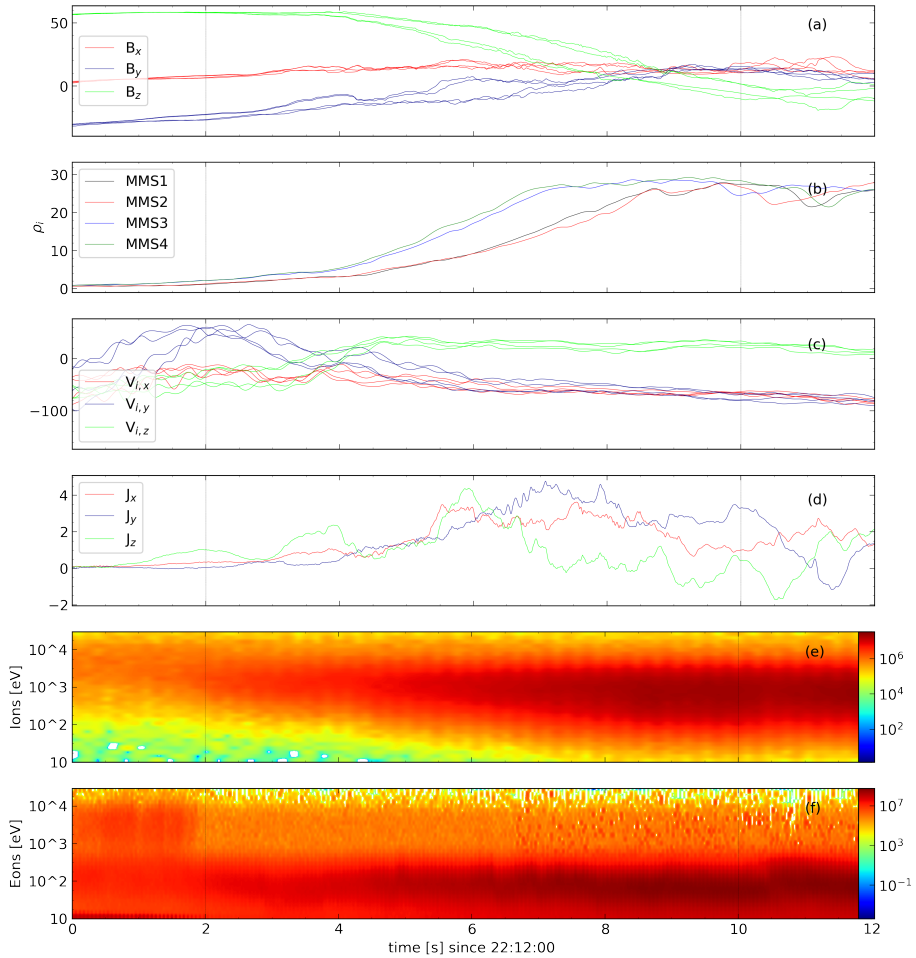


FIGURE 2. Main features of the crossing of the 28th December 2015. From top to bottom: (a) the magnetic field (in nT), (b) the ion particle density (in m^{-3}), (c) ion velocity (in km/s), (d) total current (computed from the curlmeter (Dunlop *et al.* 1988), in nA/m^2), (e) the ion and (f) electron spectrograms (energies are shown in eV). Vertical lines indicate the time interval chosen for the case study.

407 Vertical dashed lines indicate the time interval during which all the satellites are inside the
 408 boundary. We observe that the time required for the ions flux to complete the crossing (of about
 409 5s) is shorter than for the magnetic field (about 8s). To perform a quantitative analysis of the
 410 differences, we studied the angles between the different normals obtained through GF2, MDD
 411 and MVA, as shown in Fig. 4.a.

412 The first striking result is that all these results are quite consistent. Almost all the directions are
 413 less than ten degrees apart from each other, with an average difference of about five degrees. The
 414 major exception concerns the comparison between MVA and $GF2_B$ during the last second of the
 415 interval where the two directions appear to be up to 35 degrees apart. This can be explained by
 416 the fact that the local normals are observed (by $GF2_B$ as well as by MDD_B) to differ noticeably
 417 in this part from their averaged value and that MVA is not able to detect such a change. Looking
 418 in more detail, we can see a slight difference between the first part of the crossing (between
 419 2s and $\sim 6.5s$), where the two normals $GF2_B$ and MDD_B differ by less than 5 degrees, and the
 420 second part, where the angle between the normals can be up to ten degrees (probably due to a

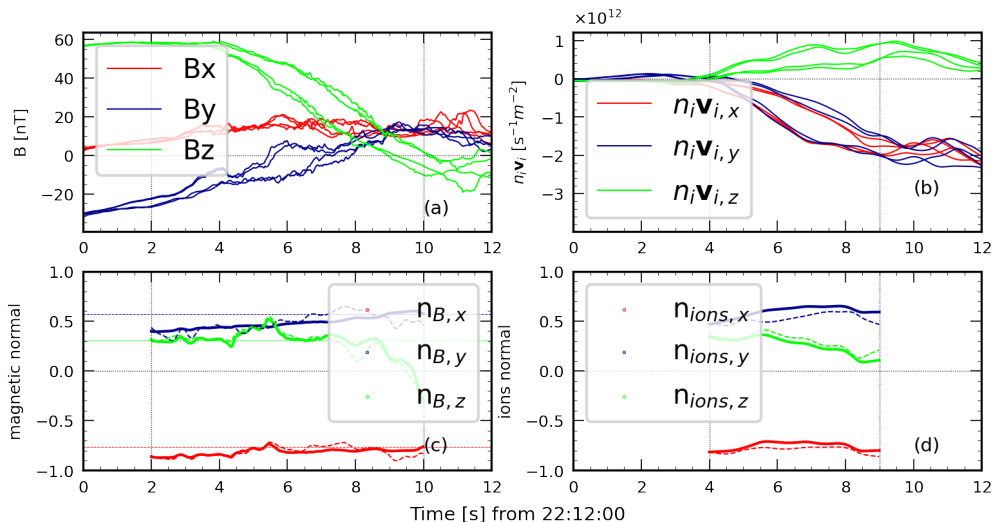


FIGURE 3. Comparison for the normals obtained with GF2 with respect to the MDD tools. (a) shows the magnetic field and (b) the ion mass flux, measured by the four MMS spacecraft. (c) and (d) shows the magnetic and the ion normal, respectively. The continuous (resp. dashed) line correspond to the components of GF2 (resp. MDD) normal. Horizontal dotted lines indicate the MVA normal obtained along the whole interval. Vertical dashed lines correspond to the time interval boundaries for the crossing, which are different for the magnetic field and the ion mass flux.

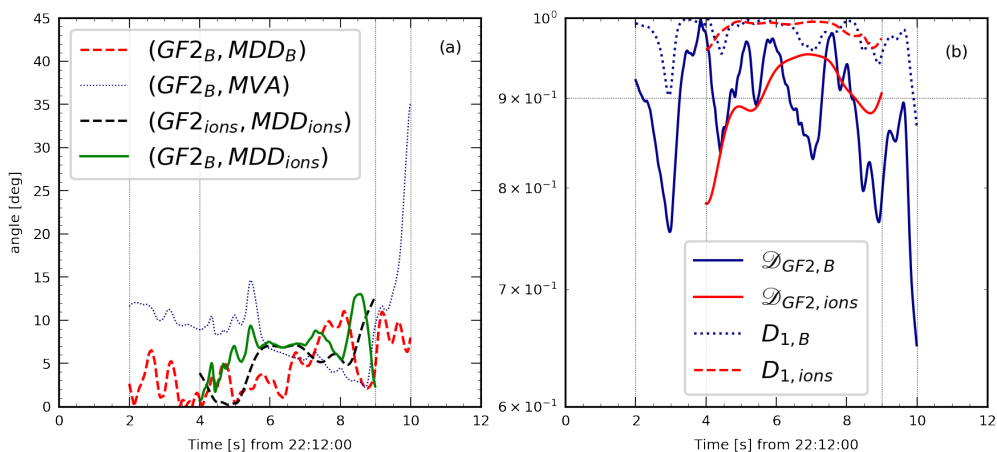


FIGURE 4. (a) Angle between the normals obtained using the state-of-the-art tools (MDD, MVA) and GF2. The subscript B and $ions$ indicates whenever the magnetic field or the ion flux measurements are used. (b) Dimensionality of the structure as a function of time; here both the \mathcal{D}_{GF2} (continuous line) and the D_1 (dashed line) indices are shown, for both the magnetic field (blue) and ions (red) data.

421 smaller ratio signal/noise for the gradient matrix \mathbf{G}). The normals derived from ion measurements
 422 are not much different from those derived from the magnetic field, showing that the particle and
 423 magnetic structures are approximately identical. In Fig. (4.b), the dimensionality of the structures
 424 is analyzed as a function of time, by using both the \mathcal{D}_{GF2} and the D_1 (Rezeau *et al.* (2018))
 425 parameters, as explained above. Even if the numerical values of the two indices are slightly
 426 different, they both indicate structures close to one-dimensionality in the first part, with a -small

Model	Normal [GSE]	angle with $\mathbf{n}_{GF2,B}$ [deg]
$\mathbf{n}_{GF2,B}$	[0.82, -0.49, -0.29]	x
$\mathbf{n}_{GF2,ions}$	[0.76, -0.59, -0.26]	7.2
MVA	[0.76, -0.57, -0.30]	6.1
MDD	[0.83, -0.49, -0.28]	0.7
Denton	[0.82, -0.49, -0.29]	0.4

TABLE 1. Magnetopause normal vectors obtained with the main tools presented above averaged in the time interval and their angle with respect to the normal obtained with GF2 using the magnetic field data (in degrees).

427 but significant- decrease in the second part. This increased departure from mono-dimensionality
 428 can explain the slight difference between the two parts when comparing the normals from
 429 standard MDD and GF2 techniques.

430 The present test does not allow us to state that GF2 is more accurate than standard MDD
 431 (this will be checked in future work by comparing the two tools in a global simulation involving
 432 realistic turbulence) but it shows at least a good agreement between the two approaches. We will
 433 see in the following that this accuracy is anyway sufficient to prove the role of FLRs.

434 In order to smooth the small fluctuations over the time interval and to reduce the statistical
 435 error associated with the determination of the normal, we can compare the directions averaged
 436 along the crossing time. Mean values obtained through the tools presented above are shown in
 437 Table 1. Here we observe that all the averaged normals differ by less than 10 degrees. Specifically,
 438 we observe that the normals obtained with GF2, MDD and (Denton *et al.* 2018) are similar, with
 439 a difference of less than one degree (with ours being closer to the one from Denton *et al.* (2018)).
 440 MVA normal, instead, differs around 6 degrees from all these other normals. Finally, we also
 441 observe that the one computed with ions flux data is the most distant. This is interpreted to be
 442 due to the higher uncertainty of particles measurements.

443 7. Case study

444 In this section, we undertake a detailed analysis of the previously mentioned crossing case by
 445 employing the normal obtained using the GF2 tool. Here, we focus on the time interval between
 446 2 s and 9 s in Fig 2. To mitigate the potential influence of non-unidimensionality effects, we chose
 447 to exclude the last second of the time interval studied in the preceding section for the magnetic
 448 field (where both \mathcal{D}_{GF2} and D_1 show that the structure is less one-dimensional and where we
 449 observe that the normal is more different from the averaged one). To carry out this analysis, we
 450 study the hodogram of the magnetic field in the tangential plane. Here the tangential results are
 451 presented in a basis ($\mathbf{T}_1, \mathbf{T}_2$) chosen as:

$$452 \quad \mathbf{T}_1 = \mathbf{n}_{mean} \times \hat{\mathbf{b}} \quad (7.1)$$

$$\mathbf{T}_2 = \mathbf{n}_{mean} \times \mathbf{T}_1 \quad (7.2)$$

453 where $\hat{\mathbf{b}} = \mathbf{B}/|\mathbf{B}|$ and \mathbf{n}_{mean} is the directions of the averaged normal in the chosen time interval.
 454 Note that the choice of the reference frame ($\mathbf{T}_1, \mathbf{T}_2$) is just a convention. The shape of the
 455 hodogram remains unaffected by this choice except for the corresponding rotation in this
 456 tangential plane. The direction \mathbf{t}_1 , which characterizes the direction of the second dimension of
 457 the model in GF2 and which is also in the tangential plane is generally different from \mathbf{T}_1 .

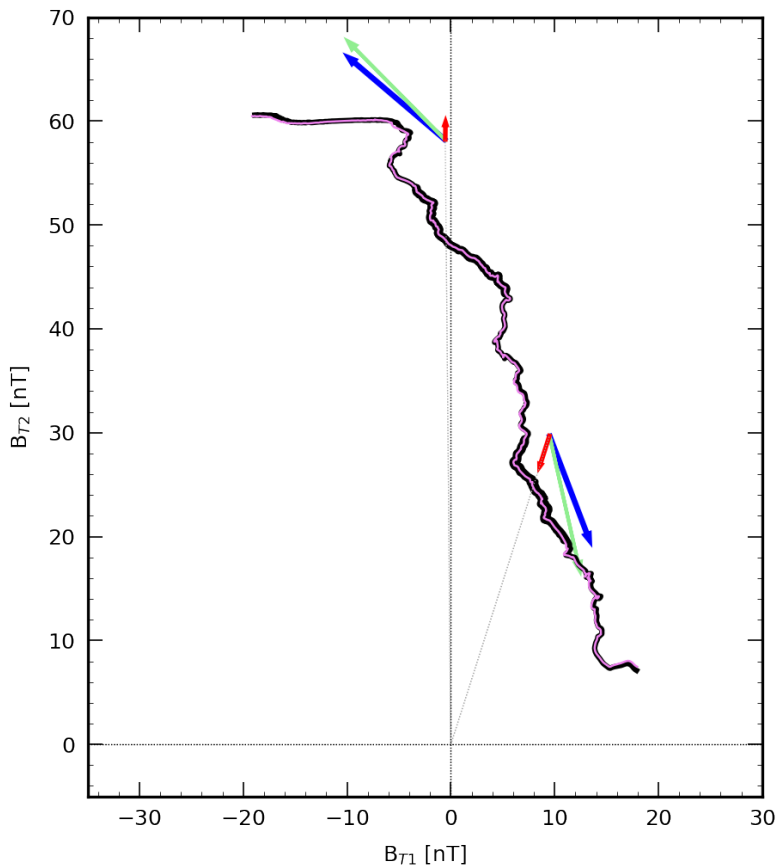


FIGURE 5. Hodogram in the tangential plane of the magnetic field for a magnetopause crossing by MMS in 28.12.2015 from 22:12:02 to 22:12:09. See text for the significance of the arrows. B_{T1} and B_{T2} are the projections of \mathbf{B} along the tangential directions computed as described in the text. The black line (resp. violet) is the hodogram when the \mathbf{n}_{mean} (resp. \mathbf{n}) value is used to define the reference frame.

458 If CTD was valid everywhere, the hodogram of the magnetic field in the tangential plane for
 459 a rotational discontinuity would correspond to a circular arc with constant radius while a shock
 460 would correspond to a radial line (as shown in Fig. 1). For this reason, the hodogram is a good tool
 461 to recognize the cases for which the CTD fails at describing the magnetopause. The hodogram
 462 for this case is shown in Fig. 5. We observe a clear "linear" (although not radial) hodogram. This
 463 non-radial variation of the magnetic field although not predicted by CTD, is a striking feature
 464 of the hodogram. It cannot be explained by a departure from the 1D assumption since we have
 465 measured that the crossing can be considered as one-dimensional to a good degree of accuracy.
 466 It is therefore due to an intrinsic property of the layer itself. Also, in Fig. 5, we present the
 467 hodogram derived from the local normal (un-averaged, violet line). It is clear that averaging does
 468 not affect the shape of the hodogram.

469 To further analyze the causes of the disagreement between the hodogram of this case
 470 crossing and what is expected from CTD, we compare the different terms of the tangential
 471 momentum equation and Faraday/Ohm's law. As discussed above, indeed, these two equations
 472 are responsible for the distinction between the rotational and tangential discontinuities in CTD.
 473 This is the object of Figure 6, where we plot the different terms of the two equations projected

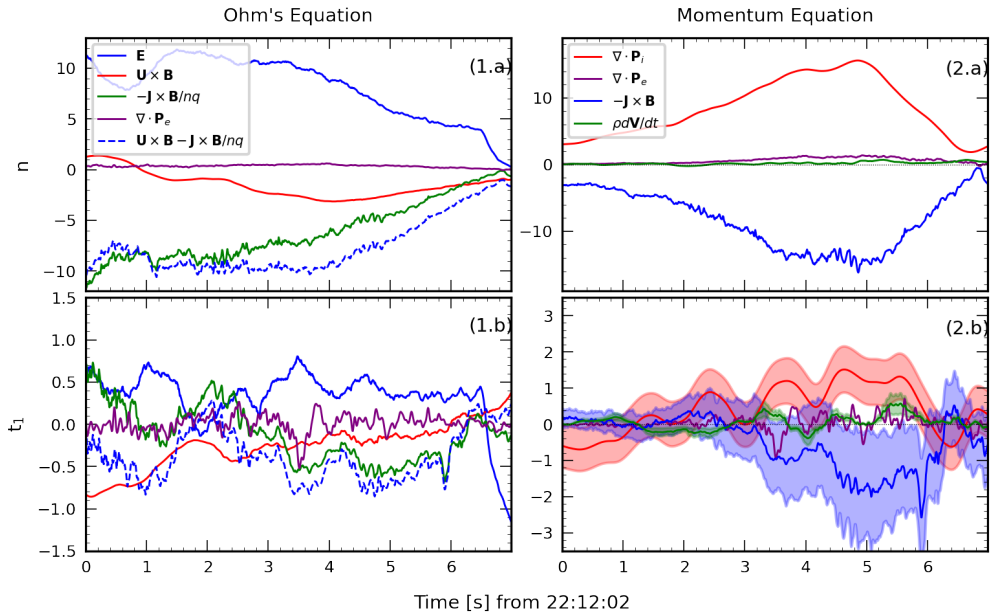


FIGURE 6. Terms of the Ohm's law (panel 1, units of mV/m) and the momentum equation (panel 2, units of 10^{-15}kg m/s^2), projected in the normal direction n (a) and in the tangential direction t_1 (b). To reduce the noise, a running average with a time window of 0.35s is applied to the electric field measurements. Shaded regions in panel 2.b represent the estimated uncertainties of the divergence of the pressure (red), the $\mathbf{J} \times \mathbf{B}$ (blue) and the classic inertial term (green). Concerning the Ohm's law, we included the sum $\mathbf{U} \times \mathbf{B} - \mathbf{J} \times \mathbf{B}/nq$ to facilitate the readability (blue dashed line).

N.b. The terms of the tangential Faraday/ Ohm's law used in the text are just the derivatives of the ones in (a) (apart from a $\pi/2$ rotation).

474 along the \mathbf{n}_{mean} and $\mathbf{t}_{1,mean}$ directions obtained using the GF2 tool (averaged over the whole
 475 time interval). The influence of the averaging of the $\mathbf{t}_{1,mean}$ direction on the results is discussed
 476 in Appendix A. We do not show the quantities along the direction of invariance, which are
 477 dominated by noise. The current and the gradient matrix for the pressure term are obtained via
 478 the reciprocal vector method described in Chanteur (1998).

479 Concerning the Ohm's law (Figure 6, panel 1), we see that the electric field is well counter-
 480 balanced by the $\mathbf{u} \times \mathbf{B}$ and $\mathbf{J} \times \mathbf{B}/nq$ terms (ideal and Hall terms). Outside the layer, on both sides,
 481 the ideal Ohm's law is satisfied, as assumed in CTD (this is not visible on the figure, which is a
 482 zoom on the inner part of the layer, and where the Hall term is important). It has been shown in
 483 the literature that $\nabla \cdot \mathbf{P}_e$ is not always negligible in the Ohm's law and that it can even be dominant
 484 close to an Electron Diffusion Regions (EDR). This has been predicted theoretically (Hesse *et al.*
 485 2011, 2014) and observed experimentally (Torbert *et al.* 2016; Genestreti *et al.* 2018), but it is not
 486 the case for events like this one. We observe that at approximately 3.5 seconds, the $\nabla \cdot \mathbf{P}_e$ is not
 487 entirely negligible along the tangential direction (a similar peak can also be observed in panel 2.b
 488 for the term associated with the electron pressure in the momentum equation). However, during
 489 this time interval, this value is not dominant, this term being smaller than both the electric field
 490 and the $\mathbf{J} \times \mathbf{B}/nq$ components. Furthermore, this effect exhibits a local characteristic, as $\nabla \cdot \mathbf{P}_e$
 491 is only non-negligible within a small sub-interval (with respect to the magnetopause temporal
 492 width). It is therefore not likely to be indicative of proximity to a reconnection point.

493 Concerning the momentum equation, shown in panel 2 of Figure 6, we observe that, in the
 494 normal direction, the $\mathbf{J} \times \mathbf{B}$ term is counter-balanced by the divergence of the ion pressure tensor,

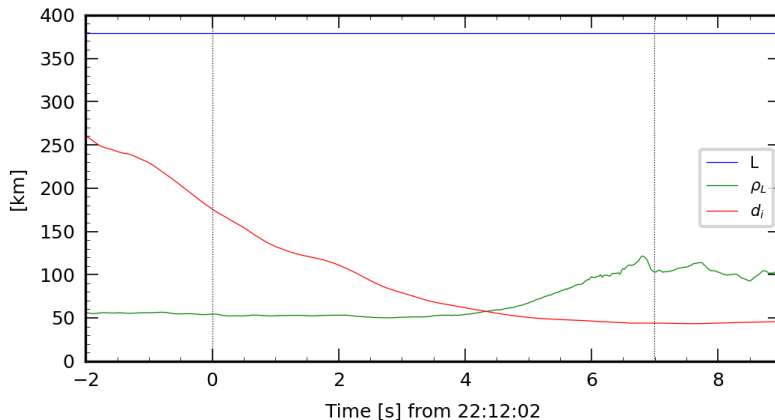


FIGURE 7. Comparison of the magnetopause width (L) with the ion inertial length (d_i) and the ions Larmor radius (ρ_L). Vertical lines highlight the considered temporal interval.

495 as expected. But, if the isotropic condition assumed in CTD was valid, we would expect the
 496 divergence of the ion pressure tensor to be zero in the tangential direction, or at least negligible
 497 with respect to the inertial term $\rho d\mathbf{u}/dt$. On the contrary, we observe that the $\mathbf{J} \times \mathbf{B}$ term along \mathbf{t}_1
 498 is of the same order of magnitude as the divergence of the ion pressure tensor, and one order of
 499 magnitude larger than all the other terms. Panel 2.b also shows an estimation of the error on the
 500 relevant terms: $\mathbf{J} \times \mathbf{B}$, $\nabla \cdot \mathbf{P}_i$ and the classical inertial term. It is known that measurements errors
 501 are difficult to estimate, especially at small scales. In order to validate our results, however, we
 502 sought to obtain an upper bound of the error associated with the quantities of interest. For that
 503 purpose, an overestimation of the uncertainty of the measurements (acquired as the maximum
 504 during the crossing of the errors available in FPI datasets for the pressure tensor and from the
 505 FGM nominal error for the magnetic field) was exploited. These values are propagated as a
 506 statistical (*i.e.* quadratic) error (by assuming that the errors on the reciprocal vectors can be
 507 neglected with respect to that of other physical quantities).

508 From panel 2.b of Fig. 6, we see that the $\mathbf{J} \times \mathbf{B}$ and the $\nabla \cdot \mathbf{P}_i$ terms are pointing in opposite
 509 directions and balancing each other. If valid in the first part of the interval, this conclusion
 510 cannot be safely trusted due to measurement uncertainty, but we observe that in the middle part
 511 (particularly between 3.5s and 6s) it is evident that the two quantities counterbalance each other
 512 while the classical inertia term $\rho d\mathbf{u}/dt$ is much lower with respect to the others. This proves that
 513 the tangent $\nabla \cdot \mathbf{P}_i$ term plays a fundamental role in the magnetopause equilibrium.

514 This point can be emphasized also by analyzing the hodogram. In Fig. 5, the arrows are
 515 directed along the directions of the tangential plane that are physically relevant for the problem:
 516 *i*) the tangent to the hodogram (green), which indicates the total variation of \mathbf{B}_t ; *ii*) the radial
 517 direction (red), which corresponds to the plasma compression; *iii*) the $\nabla \cdot \mathbf{P}_{it}$ direction (blue),
 518 which is the direction of the divergence of the ion pressure tensor in the tangential plane, and
 519 therefore corresponds to a term which is absent in CTD. The relative lengths of the arrows are
 520 chosen proportional to the corresponding term magnitudes. These directions are averaged in two
 521 sub-intervals (bold hodogram). The striking result is that the total variation is mainly determined
 522 by the non-classic term $\nabla \cdot \mathbf{P}_{it}$ and not by the radial classic one. This explains the very recurrent
 523 (even if not reported in the literature hitherto) feature that the hodograms are almost linear but
 524 not radial.

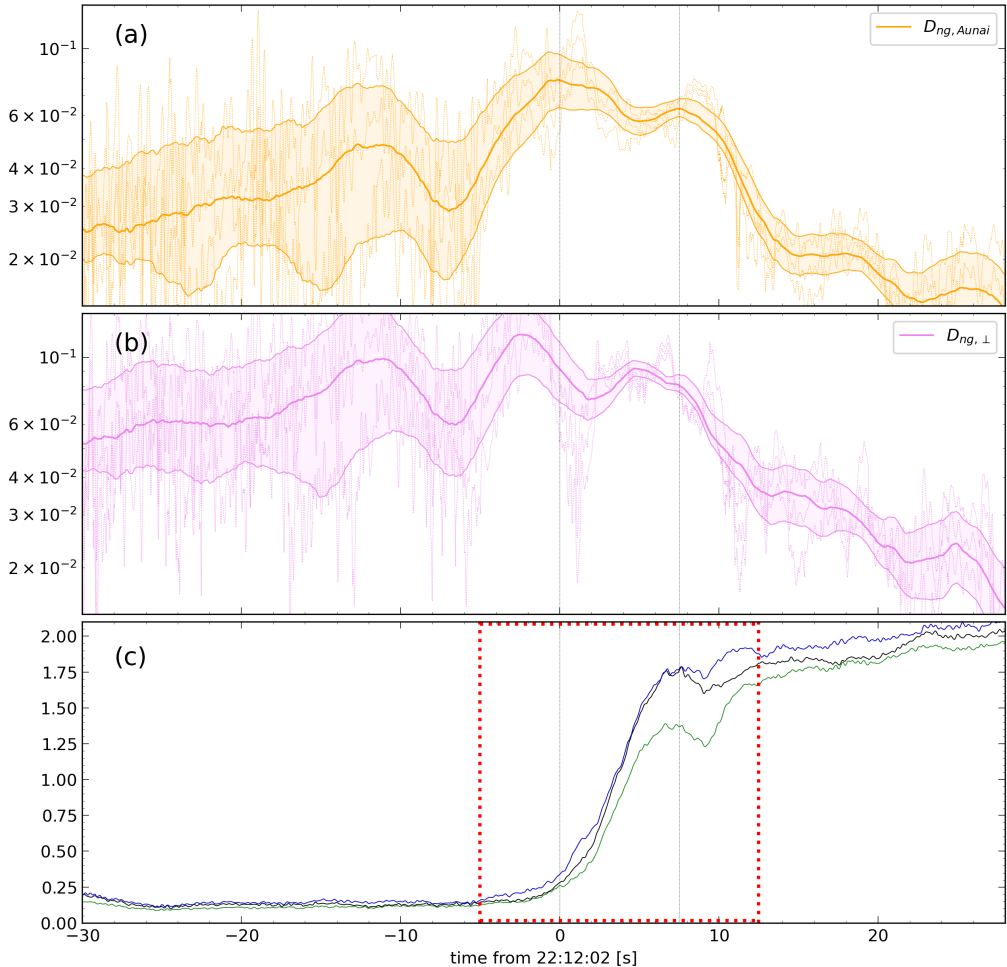


FIGURE 8. Panels *a* and *b* show the evolution of the $D_{ng,\perp}$ and $D_{ng,Aunai}$ (Aunai *et al.* 2013) indices, respectively, along with their estimated uncertainties. Thin lines correspond to the real-time values while thick lines to an averaged window of 1 s; (c) Evolution of the eigenvalues of the \mathbf{P}_i matrix (averaged on the four spacecraft). The dotted line indicates the magnetopause crossing. The red dotted lines in panel *c* highlight the time interval studied in Fig. 9

7.1. Comparison of the width of the magnetopause to relevant physical lengths

Finally, we compare the width of the magnetopause (L) to the two main ion-related lengths: the ion Larmor radius (ρ_L) and the ion inertial length (d_i). The magnetopause width is estimated using the normal velocity obtained from the *GF2* tool. By averaging the velocity of the magnetopause in the normal direction, we can estimate $L = \mathbf{V}_{n,mean}\Delta t$ (where Δt is the time length of the full crossing). These three scales are shown in Fig.7. We observe that this width is larger than the ion Larmor radius and the ion inertial length all across the crossing, but only two to five times larger, which appears sufficient to drive the observed kinetic effects.

8. Ion pressure tensor analysis

To further investigate the question of the ion non-gyrotropy with respect to the magnetic field and quantify this effect, let us now examine the properties of the ion pressure tensor and introduce

536 a new non-gyrotropy index. For that purpose, we define the matrices $\mathbf{P}_{\parallel} = p_{\parallel}\mathbf{b}\mathbf{b}$, where $\mathbf{b} = \mathbf{B}/|\mathbf{B}|$
 537 and $p_{\parallel} = \mathbf{b} \cdot \mathbf{P}_i \cdot \mathbf{b}$, and $\mathbf{P}_{\perp} = \mathbf{P}_i - \mathbf{P}_{\parallel}$. By defining p_1 and p_2 the maximum and intermediate
 538 eigenvalues of the \mathbf{P}_{\perp} matrix, we define:

$$D_{ng,\perp} = \frac{p_1 - p_2}{p_1 + p_2} \quad (8.1)$$

539 In Fig. 8.a, this parameter is compared to the non-gyrotropy index presented in Aunai *et al.*
 540 (2013). The two indices define nongyrotropy differently, (Aunai *et al.* 2013)'s index defining
 541 nongyrotropy as the ratio of the nongyrotropic to the gyrotropic part of the tensor (instantaneous),
 542 while ours makes use of the 2D modeling of the data used in GF2 (averages on sliding windows).
 543 We note how both indices are significantly different from zero, approximately of the order of 0.1
 544 within the boundary, corresponding to clearly present, although not predominant, non-gyrotropic
 545 effects. We note a decrease in both indices outside the magnetopause, as expected, but it is worth
 546 noting also that, despite a continuous decrease, these indices remain relatively high in the time
 547 interval just preceding the crossing, in a region where magnetic field, density and pressure tensor
 548 are almost constant. This can be understood by noting that an ion velocity gradient is observed in
 549 this interval, suggesting that the non-diagonal terms of the pressure tensor could be due there to a
 550 kind of gyroviscous effect, the non-diagonal terms of the pressure tensor (Braginskii 1965) being
 551 due to FLRs (Stasiewicz 1993). One must take care that, in this interval, the pressure tensor has
 552 low values characterized by larger relative errors, which could partially influence this result. To
 553 further analyze this question, we have estimated the uncertainties on both non-gyrotropy indices.
 554 This estimation is derived from the nominal uncertainties of the FPI dataset. The diagonal terms
 555 have higher values and lower relative errors. Concerning the time interval before the crossing
 556 that we discuss here, the diagonal terms have errors of approximately 5%, whereas off-diagonal
 557 terms have an average relative error about 50%. We observe on Fig. 6 that this way of estimating
 558 the uncertainty well encompasses the variance of the results. It confirms that, within the crossing
 559 interval, all relative errors are smaller than 10 %, as considered in the Ohm's law study (Fig. 6).
 560 In addition, a preliminary study appears to confirm the validity of the gyroviscous interpretation.
 561 Using the theoretical expressions given in Stasiewicz (1989), we can compare the variations of
 562 the non-diagonal terms of the pressure tensor with the spatial derivatives of the flow velocity, and
 563 evidence a fairly good correlation (see Appendix B).

564 Fig. 8 (panel *c*) also shows the evolution of the eigenvalues of the \mathbf{P}_i tensor, averaged on the
 565 four spacecraft. This figure shows how outside of the magnetopause the three eigenvalues tend to
 566 converge towards each other meaning that these media are close to isotropy. However, inside the
 567 magnetopause, we note a transition in the behavior of the intermediate eigenvalue, shifting from
 568 a value close to the minor one to being closer to the major eigenvalue. The minor eigenvalue
 569 exhibits a significant deviation from the other two towards the last part of the crossing.

570 Focusing on the temporal interval marked by the red square in Fig. 8, this transition is further
 571 investigated in Fig. 9 where we show the ions' distribution functions in the tangential plane
 572 (with respect to the magnetopause) for four different intervals during the crossing, highlighting
 573 the non-gyrotropy of the ions' distribution function over time. VDFs (printed using a linear 2D
 574 interpolation on a cartesian grid in the chosen plane using the Pyspedas library) are here averaged
 575 in the corresponding time intervals framed with the same color as in the bottom plot where the
 576 eigenvalues of the ion pressure tensor are plotted again (the time length decreases as the density
 577 increases).

578 Finally, we analyzed the non-gyrotropy with respect to a generic direction, *i.e.* without
 579 imposing that this direction is the magnetic field direction. Specifically, we have looked at a

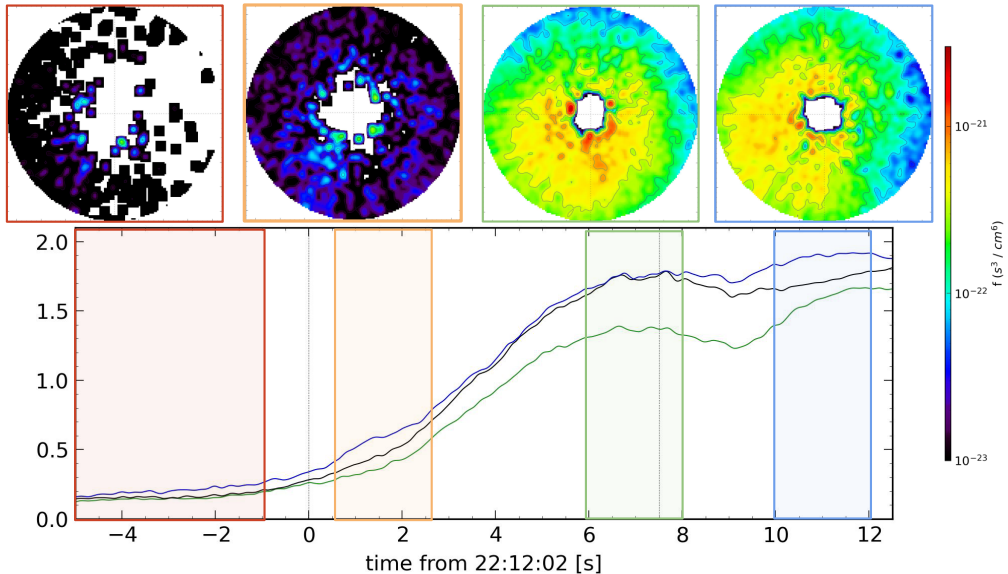


FIGURE 9. Top: Ions' velocity distribution functions in the tangential plane (the \mathbf{T}_1 - \mathbf{T}_2 plane) averaged in four different time periods. Velocities axes are between -220 km/s and 220 km/s. Bottom: Eigenvalues of the pressure tensor (same interval as in the red dashed square of Fig. 8.c). The four colored boxes are used to distinguish the four time intervals.

580 direction, denoted as \mathbf{g} , around which the rotated matrix could be rewritten as follows:

$$\begin{pmatrix} P_2 & 0 & 0 \\ 0 & P_1 & 0 \\ 0 & 0 & P_1 \end{pmatrix} \quad (8.2)$$

581 To achieve this, we employ a minimization algorithm to derive the rotation matrix \mathbf{M} that allows
 582 us to put the pressure tensor data under a form as close as possible to this one. Results from this
 583 study are shown in Fig. 10 (here shown for MMS2). Panel *a* displays the variation of P_1 and P_2
 584 along the crossing, where P_2 consistently exceeds P_1 . In addition, we imposed an upper limit on
 585 the temporal variation of the gyrotropic direction \mathbf{g} , excluding points with significant temporal
 586 variations (indicated by the thin line). Consequently, the remaining points reflect instances where
 587 the direction of \mathbf{g} can be considered as stable and reliable. The vector \mathbf{g} itself is represented in
 588 panels *b* and *c*, where it is clear that the direction of gyrotropy is not close to the magnetic
 589 field direction: it is close to $\mathbf{n}_{mean} \times \mathbf{B}$, the component along \mathbf{B} being smaller and varying. This
 590 result reminds us that at boundaries such as the magnetopause, the strong gradients can break
 591 the isotropy as much, and even more here, than the magnetic field, so that gyrotropy can be
 592 around another vector than \mathbf{B} . A similar remark had already been made in Belmont *et al.* (2012)
 593 concerning the modeling of a tangential discontinuity.

594 9. Dataset selection

595 In order to expand the results on a statistical basis, we selected a dataset of 146 crossings,
 596 chosen from the largest one reported in Nguyen *et al.* (2022) and Michotte De Welle *et al.* (2022).
 597 From this database, the following conditions were required in order to carry out an accurate
 598 study:

599 (i) MMS data are in burst mode.

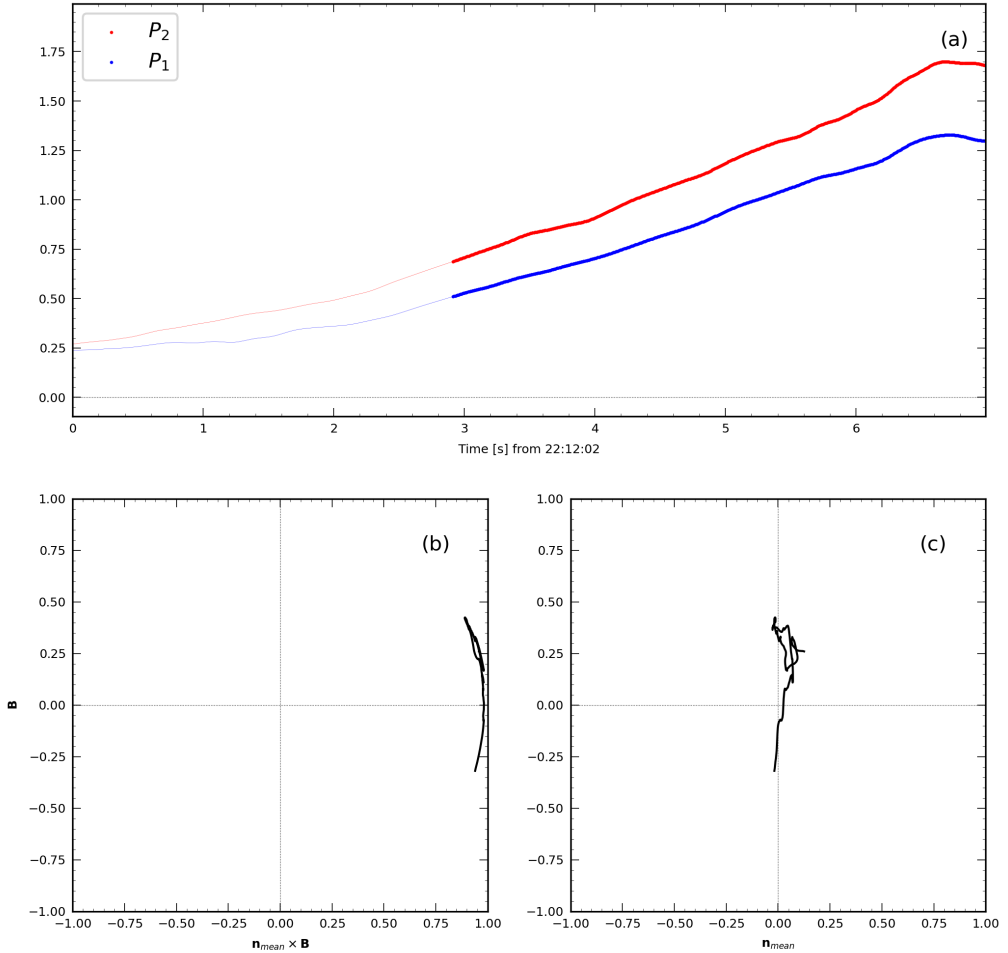


FIGURE 10. (a): Evolution of parameters P_1 and P_2 . (b) and (c): projections of the gyrotropy direction in two planes. The ordinate is the direction of \mathbf{B} , the abscissa is the direction of $\mathbf{n}_{mean} \times \mathbf{B}$ for panel (b) and \mathbf{n}_{mean} for panel (c).

- 600 (ii) The crossing duration is between 3 and 15 seconds. Too short crossings do not have a sufficient
 601 number of points within the structure (ion measurements are every 0.15 s). Too long crossings
 602 may imply non-stationary structures.
 603 (iii) Partial crossings are discarded. For that, we impose a density threshold less than 4 cm^{-3}
 604 in the magnetosphere and larger than 15 cm^{-3} in the magnetosheath.
 605 (iv) Only cases presenting simultaneous crossing features in particles and magnetic field are
 606 considered, in order to compare normals computed at the same time.

607 In addition to these basic requirements, we also excluded some of the selected crossings for
 608 criteria that demand a more detailed analysis of the internal structure of the boundary. First,
 609 we excluded two-dimensional features. The quantitative determination of the dimensionality
 610 was done with the parameters presented in Rezeau *et al.* (2018) and the dimensionality index
 611 presented in Section 5.2, which are functions of the ratio between the eigenvalues of the gradient
 612 matrix. Namely, we considered only crossings with $D_1 > 0.9$ and $\mathcal{D}_{GF2} > 0.8$, these two
 613 parameters being averaged on the crossing interval. These parameters are calculated at each time

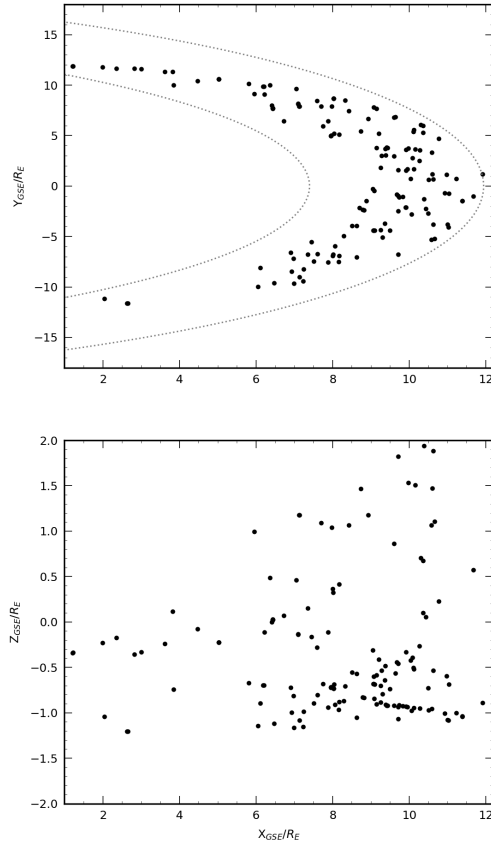


FIGURE 11. Spatial distribution of the selected database of crossings on the x, y (top) and x, z planes (bottom). The dashed grey lines represent the magnetopause location (Shue *et al.* 1997).

614 step but, due to waves and turbulence, attention must be paid that some of these two-dimensional
 615 features can be only local and insignificant for the profiles we are looking for. It is the reason
 616 why we use only the averaged values. The 146 selected crossings span from September 2015 to
 617 December 2017 (included). We can observe in Figure 11 that the crossings are evenly distributed
 618 in the x, y plane. Regarding the z component, there is a prevalence of cases at negative z .

619 The list of crossings can be found in Supplementary Materials. For each crossing, the
 620 classification and the physical quantities relevant for the study (normals, dimensionality index,
 621 non-gyrotropy index, and the main characteristic lengths discussed above for the case crossing)
 622 are included.

623 10. Statistical study of the magnetic hodograms

624 The previous results about the role of the FLR effects at the magnetopause are now carried out
 625 statistically. This study aims to generalize the results obtained from the case crossing studied in
 626 the previous section and to estimate the role played by FLRs at the magnetopause.

627 The database described above has first been used to perform a statistical study on the hodogram
 628 shapes, to determine how often linear hodograms are observed in magnetopause crossing. Having
 629 an estimation of the percentage of crossings that do not conform to CTD allows us to gauge how
 630 frequently the assumptions made by this theory do not accurately represent the magnetopause.

631 For this purpose, we separate the crossings in different classes, this classification being based on
 632 CTD distinctions and on the preceding findings:

- 633 (i) *Linear* crossings, *i.e.* straight lines not passing through the origin as in the above case study.
- 634 (ii) *Radial* crossings, including all linear crossings whose best fit line passes through the origin
 635 (considering uncertainty). These crossings correspond to CTD compressional discontinuities.
- 636 (iii) *Circular* crossings, when the distance from the origin is constant. These cases correspond to
 637 CTD rotational discontinuities.
- 638 (iv) *Other* crossings, whose features are not included in the previous classes. This class includes
 639 crossings with various features, *e.g.* circular hodograms not centered on the origin, crossing
 640 characterised by two different hodograms in two sub-intervals, etc., and crossings that do not
 641 have an obvious distinction between the previous classes, due to noise.

642 To classify each crossing, we only focus on its central time interval, where the gradients
 643 are maximum. By considering larger time intervals, the hodograms' shape becomes more
 644 complex because the variations out of this interval are generally unrelated to the main boundary
 645 jumps. Selecting only the middle part of the crossing provides simpler and more conformal
 646 hodograms. Even if the boundary jumps are not fully completed in this part, this will not prevent
 647 comparing the experimental results with CTD predictions since this theory, when valid, is
 648 based on conservation laws for any sub-interval of the discontinuity. When this theory fails to
 649 reproduce the observed properties, we can interpret those new features as coming from kinetic
 650 effects, therefore confirming the limitation of CTD to describe the magnetopause boundary. To
 651 that purpose, for each dataset we selected the crossing temporal interval following the algorithm
 652 used in Haaland *et al.* (2004, 2014) and Paschmann *et al.* (2018b) to estimate the spatial scale of
 653 the magnetopause (intervals are identified as 75% of the magnetic field \mathbf{B}_L component variation).

654 The classification performed here differs from previous attempts to classify magnetopause
 655 hodograms, as seen in studies such as Sonnerup & Ledley (1974); Berchem & Russell (1982)
 656 and Panov *et al.* (2011). In these previous works, hodograms were categorized as C-shaped
 657 or S-shaped based on their form in the tangential plane. However, unlike those studies, we
 658 considered the central part of the crossing, rather than considering the entire temporal interval.
 659 Our classification of hodograms involves a two-step process:

- 660 (1) Visual Inspection: Initially, all hodograms are visually inspected to identify the cases that
 661 are clearly not linear or circular, which are classified separately as 'Others'. Additionally, a
 662 preliminary distinction is made between crossings with circular and linear features.
- 663 (2.a) Analysis of hodograms with possible circular features: For these crossings, we analyze
 664 the variation of the modulus of the magnetic field in the plane, allowing for a maximum
 665 possible variation of 20%. This accounts for factors such as turbulence and waves propagating
 666 alongside the magnetopause. Any crossings exceeding this 20% threshold are categorized as
 667 'Others.'
- 668 (2.b) Analysis of hodograms with possible linear or radial features: These crossings undergo an
 669 initial assessment to confirm their linearity. This involves examining the width-to-length ratio
 670 of the crossing, with any ratio exceeding 20% classified as 'Other.' Finally, the remaining
 671 crossings are classified as either radial or linear based on whether their projection passes
 672 through the origin.

673 From this database, we found the following distribution:

- 674 - 36.3% (53/146) of the crossings present linear features.
- 675 - 2.7% (4/146) of the crossings present circular features (rotational discontinuity).
- 676 - 15.8% (23/146) of the crossings present radial features (compressional discontinuity).

677 - 45.2% (66/146) of the crossings could not be interpreted definitely as either of the three before
678 (presenting more than one feature at the same time).

679 It follows that more than a third of the selected crossings show linear features, emphasizing
680 that the fundamental role FLR effects have on magnetopause structure is found in a significant
681 number of crossings.

682 It could be interesting to compare the above results with the several classifications that were
683 previously published (see Liu *et al.* (2022) and references therein). These previous classifications
684 were not based on the analysis of the rotational and compressional properties as done here, but
685 on the normal component of the magnetic field and its magnitude (background and variation)
686 (Smith 1973; Burlaga *et al.* 1977; Tsurutani & Smith 1979; Neugebauer *et al.* 2010). For such a
687 comparison, however, one should take care that there are important differences in the definitions:
688 in these previous classifications in particular, any discontinuity is named "tangential", whatever
689 its other properties, as soon as the measured B_n is sufficiently smaller than B , the threshold for
690 this ratio being for instance of the order of 0.3 (Liu *et al.* 2022; Smith 1973; Burlaga *et al.* 1977;
691 Tsurutani & Smith 1979; Neugebauer *et al.* 2010). This is of course a very different approach
692 from the one we use here since, even when B_n is small (and even if barely measurable), we
693 consider that different kinds of discontinuities exist, with different properties.

694 As done for the case study above, it was possible to study on a statistical basis *i*) the ratio
695 between the width of the magnetopause and the ion Larmor radius and *ii*) the non-gyrotropy
696 index. For both parameters, the case study appears rather typical. On average, the magnetopause
697 was found to be approximately 6.5 times the ion Larmor radius, only slightly smaller (6.1) for
698 linear hodograms. Similarly, the non-gyrotropy index $D_{ng,\perp}$, has an average value of 0.07, only
699 slightly higher (0.08) for linear hodograms. The $D_{ng,Aumai}$ index has even comparable averages for
700 the four different classes. It therefore seems that, although non gyrotropy has been demonstrated
701 above to play an important role, the non-gyrotropy index alone is not decisive for predicting
702 unequivocally the shape of the hodograms. This question should be the subject of future works.

703 11. A comparison between the magnetic and the particles normals

704 For each crossing, both the magnetic and the particles normals were computed with the
705 GF2 tool. Thanks to the high resolution of the MMS measurements, we can measure the local
706 fluctuations of the normals inside the magnetopause around their mean values. However, in order
707 to compare the magnetic and ion geometries, a single average normal was used for each case.
708 The mean normal is obtained inside the same time interval as in the previous study.

709 To study the differences between the two normals, we compared them via their departure from
710 the Shue model's normal (where the magnetopause is assumed to be a paraboloid, (Shue *et al.*
711 1997)). This normal was obtained using the solar wind and IMF properties from the OMNI data
712 set (King & Papitashvili 2005). The time delay between the crossing time and the measurement
713 time of the solar wind relevant parameters is estimated by using the propagation method used
714 in Michotte De Welle *et al.* (2022) (which was adapted from Šafránková *et al.* (2002)). The
715 procedure for acquiring these parameters is as follows: *i*) the distance from the bow shock's nose
716 (where OMNI data are defined) to the crossing location, projected along the Earth-Sun axis,
717 is estimated; *ii*) we estimate the solar wind's propagation time (t_{est}) between these two points,
718 assuming an average solar wind velocity of 400 km/s; *iii*) the solar wind velocity V_{sw} is then
719 determined from the OMNI dataset, averaging over a 2-minute interval centered on the crossing
720 time adjusted by the time delay t_{est} ; and (IV) ultimately, a final time delay is computed based on
721 V_{sw} , which is subsequently utilized to obtain final values of solar wind and IMF parameters. The
722 crossings for which OMNI data computed with this procedure are missing (10 out of 146) were
723 left out of this analysis.

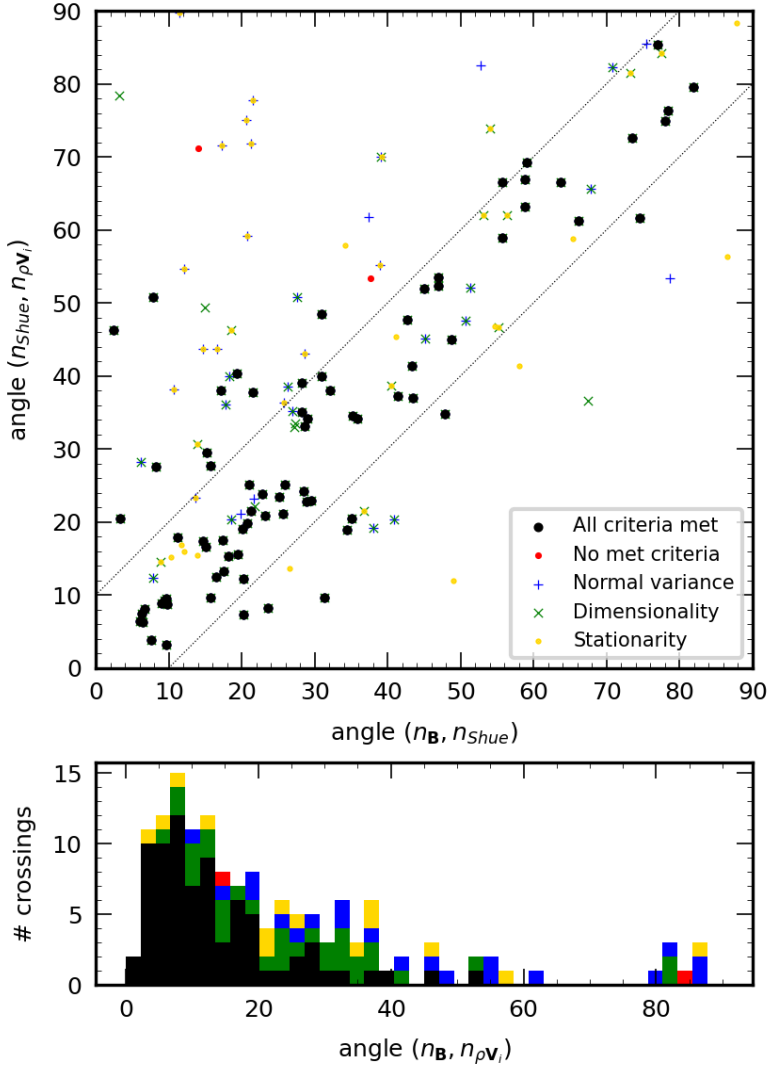


FIGURE 12. (a) Comparison between the angle between the theoretical normal (Shue *et al.* 1997) and the magnetic and ion normals, (b) Distribution of the angle between the magnetic and ion normals. Here the markers for each point is chosen depending on whether each crossing respects the criteria on dimensionality, stationarity, and normal variance on the ions flux measurements (see Appendix C for further details). Colors in the histograms are used accordingly. Blue, green and yellow points indicate the crossing with small variance on the ions normal direction within the crossing, good one-dimensionality and good stationarity. Black points indicate the crossings respecting all criteria, red points not any criteria.

724 In Figure 12.a, we plot the angle between the nominal normal and the magnetic and particles
 725 normals respectively. In this figure we observe that most of the crossings are along the diagonal,
 726 corresponding to cases where the two normals, ionic and magnetic, are similar (82 points out of
 727 146 are between the two thin lines, which indicate differences of $\pm 10^\circ$).

728 The cases are distributed throughout the plane, with many cases above 40° , although we
 729 observe a cluster at lower angles, between zero and 30° . The largest angles correspond to a
 730 magnetopause very far from the paraboloid shape assumed in Shue's model, which relies on the

731 assumption of a magnetopause at (or near) equilibrium. The departures are likely to be related to
 732 surface waves on the boundary itself.

733 Finally, the distribution of the angles between the two normals is shown in Fig. 12.*b*. Here we
 734 evidence again that most of the cases studied (82 out of 146) are below 20° , with the maximum
 735 of the distribution at 10° . However, we also observe again that several cases have much larger
 736 angles, up to 90° . The strongest departures are problematic and deserve further investigation.
 737 This appears to be due to the more complex ion structure with respect to the magnetic one. As the
 738 criteria used for the dataset selection were built from magnetic data, they are not as relevant when
 739 considering ion normals. This is evidenced in Figure 12, where the colors indicate how several
 740 ion criteria are satisfied. These criteria concern respectively the dimensionality, the stationarity,
 741 and the variance of the normal direction. All details are given in Appendix C. Focusing on points
 742 respecting all the criteria for the ions flux (black markers and hodogram), we observe that only a
 743 few crossings are outside the diagonal. Only two of these crossings have angles above 40° .

744 12. Conclusions

745 The study of the properties of the magnetopause is a very important issue for understanding
 746 the penetration of the solar wind plasma into the magnetosphere. In the theoretical part, we
 747 show that the notion of "quasi-tangential" discontinuity has to be introduced to complete the
 748 theory of discontinuities and understand the limit when the crossing fluxes tend to zero as in
 749 the magnetopause case. We emphasize that, in presence of anisotropy, the physical processes
 750 occurring inside the layer play a fundamental role because they are responsible for the conditions
 751 linking the downstream and upstream quantities. In particular, for thin current layers, the FLR
 752 corrections corresponding to the non-gyrotropic pressure tensor components must be taken into
 753 account.

754 The tool GF2 presented in the paper and used for determining the normal direction to the
 755 boundary derives from the MDD method. It includes in addition a fitting procedure, which allows
 756 introducing a part of the temporal information via a 4-point filtering of the data and adding
 757 constraints such as $\nabla \cdot \mathbf{B} = 0$. It is shown here to provide results quite compatible with the
 758 original method (when used with smoothed data), which is enough for drawing reliable physical
 759 conclusions on the magnetopause equilibrium. We expect that this approach could bring more
 760 precise information concerning the magnetopause gradients. Unfortunately, investigating this
 761 point in more detail cannot be done using MMS data but requires testing the tool in fully 3D
 762 kinetic simulations with realistic turbulence. This point is the subject of future work. Here, we
 763 have applied this tool on a particular crossing case and compared with other state-of-the-art
 764 normals. We have shown that the local normal (at each time step during the crossing) differs by
 765 less than ten degrees from the one calculated by all the other models. When averaging over the
 766 whole crossing, the normal obtained with the GF2 is even less than one degree apart from the
 767 normals from Shi *et al.* (2005); Denton *et al.* (2018).

768 Although we cannot claim to have achieved the ideal accuracy of about one degree, the reached
 769 accuracy is sufficient to evidence the correct physics at play, resumed as FLR effects. We have
 770 presented the results for a crossing observed by the four MMS spacecraft. For this crossing,
 771 the "linear" hodogram in the tangential plane shows that the boundary properties differ from
 772 those predicted by CTD. This discrepancy is explained by looking at the tangential components
 773 of the momentum equation, which highlights the role of the pressure tensor symmetries in the
 774 magnetopause equilibrium. This result agrees with the theoretical results of the first part and it is
 775 likely to hold more generally for all quasi-tangential discontinuities. The ion pressure tensor has
 776 been analyzed for this purpose. We have used two indices of non-gyrotropy, which both confirm
 777 the presence of a significant, even if small, non-gyrotropic part in this tensor. Furthermore,
 778 we have shown that the non-gyrotropy direction differs from the magnetic field one, aligning

779 approximately with the $\mathbf{n}_{mean} \times \mathbf{B}$ direction. Finally, the analysis of the VDFs directly confirms
780 the presence of non-gyrotropic distributions.

781 To show that our methodology applies to cases that CTD cannot handle, we have selected a
782 substantial number of magnetopause crossings with one-dimensional characteristics to have a
783 proper statistical basis for our findings. For all these crossings, we have plotted the hodogram
784 of the magnetic field in the tangential plane and classified them depending on their geometry.
785 Our results show that 36.3% of the crossings evidence clear linear features, incompatible with
786 the CTD description, while only 18.5% of the crossings show either circular or radial hodograms
787 as predicted by CTD. In other words, a significant number of cases escapes the classic theory,
788 proving that the relevance, even if not a predominance, of FLR effects at the magnetopause can
789 be generalized and that the case crossing presented in the first section is rather typical. It is well-
790 known that the linear version of the rotational discontinuity is the MHD shear Alfvén wave. Here
791 it appears that the magnetopause-like "quasi-tangential" discontinuities correspond in the same
792 way to the quasi-perpendicular "Kinetic Alfvén Waves" (Hasegawa & Uberoi 1982; Belmont &
793 Rezeau 1987; Cramer 2001).

794 Several papers have investigated the changes in rotational discontinuities when various non-
795 ideal effects are introduced. These theoretical papers have addressed the problem as a Riemann
796 problem using the methodology of a "piston" to study the formation of different discontinuities.
797 Some introduced FLRs and gyroviscosity in the layer while assuming isotropy on both sides
798 (Lyu & Kan 1989; Hau & Sonnerup 1991), and others introduced anisotropy everywhere while
799 assuming gyrotropy in the layer (Hau & Wang 2016). These different papers lead to different
800 conclusions; in particular concerning the role of electron inertia in the layer equilibrium.

801 It is worth noticing that the hodograms of \mathbf{B} obtained with these theoretical studies were never
802 far from circular ones, contrary to the almost linear shapes shown in the present paper. Our
803 methodology has been different here: without assuming pre-defined forms for the non-ideal
804 terms, we look experimentally to the hodograms and the form of the \mathbf{P} tensor and explain
805 theoretically how the second can explain the first ones.

806 Finally, we have used the same database of crossings to compare the geometric properties
807 of the magnetic and ion structures. We have compared the normal obtained from the magnetic
808 field and the ion flux measurements to the one expected from Shue *et al.* (1997) model. Many
809 crossings differ by more than 40 degrees from the nominal equilibrium condition, underlining a
810 very dynamical environment, but it is worth noticing that the two kinds of determination are most
811 often in agreement with each other, and therefore confirm the result. Furthermore, an accurate
812 study of the ion flux measurements have shown that crossings showing bigger discrepancies
813 between the magnetic field and ion flux normals are generally due to non-stationarities, non-one-
814 dimensionality, or variations in the ion flux normals. When excluding these cases from the study,
815 the ion and magnetic flux normals are compatible with only two crossings (over 77) showing
816 angles larger than forty degrees.

817 Data availability

818 Magnetospheric Multiscale satellite data were accessed through the MMS Science
819 Data Center, <https://lasp.colorado.edu/mms/sdc/public/>. Furthermore, all the
820 softwares employed, from interpolation of the data to the analysis itself, can be found at
821 https://github.com/GiulioBallerini/Notebooks_FLR.git.

822 **Acknowledgements:** The authors strongly thank Nicolas Aunai and Bayane Michotte de Welle
823 for useful discussions. The French involvement on MMS is supported by CNES and CNRS.

824 **Declaration of interests:** The authors report no conflict of interest.

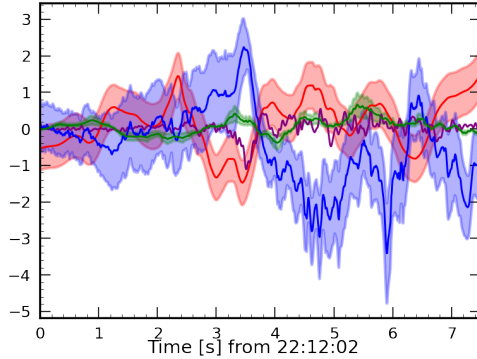


FIGURE 13. Terms of the momentum equation (units of 10^{-15}kg m/s^2), projected on the local tangential direction (\mathbf{t}_1). Shaded regions are estimated uncertainties of the divergence of the pressure (red), the $\mathbf{J} \times \mathbf{B}$ (blue) and the classic inertial term (green).

825 **Funding:** The first author, Giulio Ballerini, acknowledges the support of "Ecole Franco-
826 Italienne" (grant number C2-222)

827 **Appendix A. Influence of averaging the \mathbf{t}_1 direction in the momentum equation** 828 **balance**

829 In this section, we investigate the impact of using an averaged tangential direction along the
830 crossing on the outcomes concerning the role of the pressure tensor in the momentum equation.
831 In Fig. 13 we show the projection of the terms of the momentum equation along the local \mathbf{t}_1
832 direction (*i.e.* without averaging). We observe here some reversals of the sign of the dominant
833 terms, that were not observed in the averaged case. Nonetheless, it is still evident that the pressure
834 tensor counterbalances the $\mathbf{J} \times \mathbf{B}$ term, hereby confirming our earlier findings.

835 **Appendix B. Analysis of the gyroviscous effects**

836 In this section, we use the magnetopause crossing analysed in detail above to study the validity
837 of the gyroviscous interpretation. In particular, we employ the Braginskii gyroviscosity term
838 (Braginskii 1965) as applied by Stasiewicz (1989) to the magnetopause, to analyze the pressure
839 tensor. In this case, the pressure tensor is considered as the sum of an isotropic component, \mathbf{P}_{iso}
840 and a viscosity term, σ :

$$\mathbf{P}_i = \mathbf{P}_{iso} - \sigma \quad (\text{B } 1)$$

841 To investigate the viscosity term, we use the reference system where the normal direction is
842 aligned with the z-axis (the x and y directions are chosen accordingly to form an orthogonal
843 triad). By exploiting the definition of σ , we focus here on its projection along the normal yielding
844 the following relation:

$$-\sigma \cdot \mathbf{n} = \begin{pmatrix} P_{nx} \\ P_{ny} \\ P_{nz} \end{pmatrix} = \rho \nu \begin{pmatrix} 0 & b_n & b_y \\ -b_n & 0 & -b_x \\ b_y & -b_x & 0 \end{pmatrix} \cdot \begin{pmatrix} u'_x \\ u'_y \\ u'_n \end{pmatrix} \quad (\text{B } 2)$$

845 Here ν is the gyroviscosity coefficient, $\hat{\mathbf{b}} = (b_x, b_y, b_z)$ the normalized magnetic field, and $\mathbf{u}' =$
846 (u'_x, u'_y, u'_z) is the vector of the spatial derivatives of the velocity components along the normal.
847 We now consider the first two components of this equation, yielding the following expressions

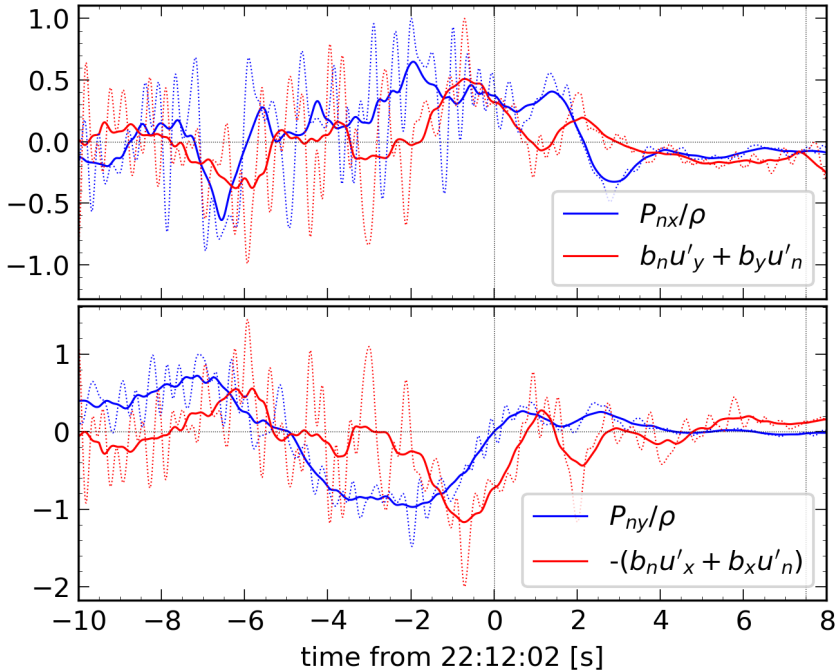


FIGURE 14. Left (blue) and right (red) hand sides for Equations B 3 (top) and B 4 (bottom). Thin-dotted lines correspond to the real-time values while thick lines to an averaged window of 1 s. All terms are normalized.

848 that allow us to compare the non-diagonal terms with the velocity changes:

$$\frac{P_{nx}}{\rho} = v(b_n u'_y + b_y u'_n) \quad (\text{B } 3)$$

849

$$\frac{P_{ny}}{\rho} = -v(b_n u'_x + b_x u'_n) \quad (\text{B } 4)$$

850 The terms of these equations are shown (normalized) in Figure 14. Here we observe a fairly good
 851 correlation between the non-diagonal terms of the pressure tensor and the spatial derivatives of
 852 the flow velocity.

853 Appendix C. Quality indices for the ion normals

854 In the absence of additional caution, Figure 12 shows that the angle between the normal
 855 obtained with the magnetic field and the one with the ion flux reaches very high values, up to 90
 856 degrees. This result requires a more accurate study, as the criteria used for the dataset selection
 857 are based on the magnetic field (except for the threshold imposed on the density values).

858 To interpret the results accurately, the following parameters were considered:

- 859 (i) Dimensionality of ion flux. For this purpose, we exploit the dimensionality index defined in
 860 Equation 5.11, computed from the ion flux measurements.
- 861 (ii) Stationarity of the ion flux measurements. To evaluate stationarity, we exploit the GF2 tool.
 862 Specifically, we consider the quality of the fit of the gradient matrix as an index of stationarity.

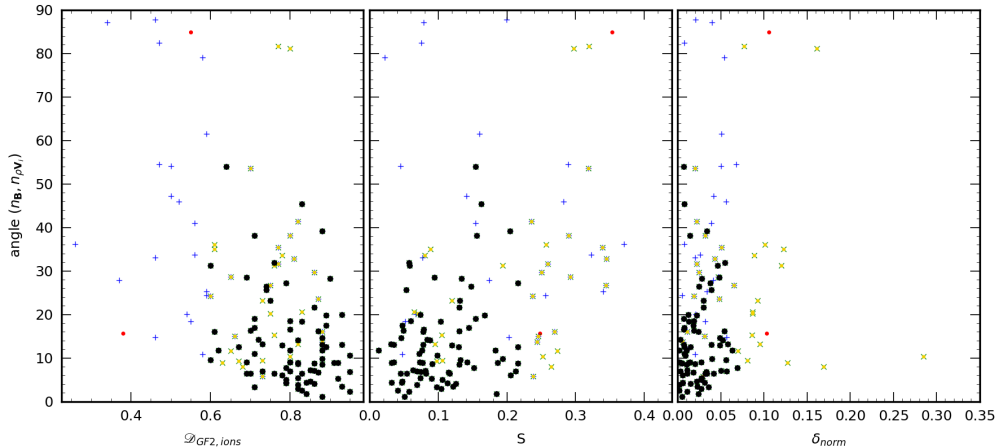


FIGURE 15. Dimensionality (left), stationarity (center), and normal variance (right) averaged for each crossing as a function of the angle between the magnetic field normal and the ion flux one. Green, blue, and yellow indicate crossings respecting the $\mathcal{D}_{GF2,ions} > 0.6$, $\delta_{norm} > 0.07$, $S > 0.22$ criteria individually. Black dots indicate the crossings for which all the criteria are met, and red dots (two cases) when no condition is met.

863 By defining $\mathbf{D} = \mathbf{G}_{fit} - \mathbf{G}$ we can introduce the stationarity index:

$$S = \frac{\text{Tr}(\mathbf{D}\mathbf{D}^T)}{\text{Tr}(\mathbf{G}\mathbf{G}^T)} \quad (\text{C } 1)$$

864 Since for a truly stationary magnetopause, S should be equal to zero, deviations from zero
865 suggest potential non-stationarity.

866 (iii) Variance of the normal. In some crossings of the database, the normal associated with ion
867 flux exhibits local differences with respect to the mean value, such as fluctuations or rotations
868 within a plane, with one component varying within the crossing. In these cases, the ion flux is
869 therefore characterized by more complex structures and the mean normal is not meaningful.
870 To exclude such cases, we examined the variation of the normal around the mean value,
871 defined as follows:

$$\delta_{norm} = \langle |\mathbf{n}_i - \mathbf{n}_{mean,i}|^2 \rangle \quad (\text{C } 2)$$

872 Small values of δ_{norm} indicate almost constant normals.

873 The average values of these three parameters for each crossing are shown in Figure 15 as a
874 function of the angles between the normal of the magnetic field and the ion flux. We observe
875 here that crossings showing the largest angles occur when at least one of these conditions fails.
876 To select the cases for which the ions are characterized by a stationary and one-dimensional
877 structure, for which the normal has no variations around the mean value, we applied the following
878 thresholds: $\mathcal{D}_{GF2,ions} > 0.6$, $\delta_{norm} > 0.07$, $S > 0.22$. Specifically, crossings individually meeting
879 one of these criteria are shown in green, blue, and yellow, respectively. When all criteria are met,
880 crossings are indicated by black dots. This Figure underlines a correlation between the difference
881 between the two normals and the values of these three parameters, showing how cases with higher
882 $\mathcal{D}_{GF2,ions}$ and smaller δ_{norm} and S are the ones with smaller differences between the two normals.

REFERENCES

883 ABRAHAM-SHRAUNER, BARBARA 1967 Propagation of hydromagnetic waves through an anisotropic plasma.
884 *Journal of Plasma Physics* **1** (3), 361–378.

- 885 AUNAI, NICOLAS, HESSE, MICHAEL & KUZNETSOVA, MARIA 2013 Electron nongyrotropy in the
 886 context of collisionless magnetic reconnection. *Physics of Plasmas* **20** (9), 092903, arXiv:
 887 <https://doi.org/10.1063/1.4820953>.
- 888 AUNAI, N., HESSE, M., LAVRAUD, B., DARGENT, J. & SMETS, R. 2016 Orientation of the X-line in asymmetric
 889 magnetic reconnection. *Journal of Plasma Physics* **82** (4), 535820401.
- 890 AUNAI, N., RETINÒ, A., BELMONT, G., SMETS, R., LAVRAUD, B. & VAIVADS, A. 2011 The proton pressure tensor
 891 as a new proxy of the proton decoupling region in collisionless magnetic reconnection. *Annales*
 892 *Geophysicae* **29** (9), 1571–1579.
- 893 BELMONT, G., AUNAI, N. & SMETS, R. 2012 Kinetic equilibrium for an asymmetric tangential layer. *Physics*
 894 *of Plasmas* **19** (2), 022108.
- 895 BELMONT, GÉRARD, GRAPPIN, ROLAND, MOTTEZ, FABRICE, PANTELLINI, FILIPPO & PELLETIER, GUY 2014
 896 *Collisionless plasmas in astrophysics*. Wiley.
- 897 BELMONT, G. & REZEAU, LAURENCE 1987 Finite Larmor radius effects: the two-fluid approach. *Annales*
 898 *Geophysicae* pp. vol. 5, no2, pp. 59–69.
- 899 BELMONT, GÉRARD, REZEAU, LAURENCE, RICONDA, CATERINA & ZASLAVSKY, ARNAUD 2019 *Introduction to plasma*
 900 *physics*. ISTE Press.
- 901 BERCHEM, JEAN & RUSSELL, C. T. 1982 Magnetic field rotation through the magnetopause: ISEE 1 and 2
 902 observations. *Journal of Geophysical Research: Space Physics* **87** (A10), 8139–8148.
- 903 BERTUCCI, C. 2005 Structure of the magnetic pileup boundary at mars and venus. *Journal of Geophysical*
 904 *Research* **110**, A01209.
- 905 BRAGINSKII, S. I. 1965 Transport Processes in a Plasma. *Reviews of Plasma Physics* **1**, 205, aDS Bibcode:
 906 1965RvPP...1..205B.
- 907 BURCH, J. L. & PHAN, T. D. 2016 Magnetic reconnection at the dayside magnetopause: Advances with mms.
 908 *Geophysical Research Letters* **43** (16), 8327–8338.
- 909 BURLAGA, L. F., LEMAIRE, J. F. & TURNER, J. M. 1977 Interplanetary current sheets at 1 AU. *Journal of*
 910 *Geophysical Research* **82** (22), 3191–3200.
- 911 CHANTEUR, GÉRARD 1998 Spatial interpolation for four spacecraft: Theory. *ISSI Scientific Reports Series 1*,
 912 349–370, ADS Bibcode: 1998ISSIR...1..349C.
- 913 CHAO, J.K. 1970 *Interplanetary collisionless shock waves*. Vita. Bibliography: leaves 148-150. Sc D.
- 914 CHASAPIS, A., RETINÒ, A., SAHRAOUI, F., VAIVADS, A., KHOTYANTSEV, YU. V., SUNDKVIST, D., GRECO, A.,
 915 SORRISO-VALVO, L. & CANU, P. 2015 THIN CURRENT SHEETS AND ASSOCIATED ELECTRON
 916 HEATING IN TURBULENT SPACE PLASMA. *The Astrophysical Journal* **804** (1), L1.
- 917 COATES, A.J. 1997 Ionospheres and magnetospheres of comets. *Advances in Space Research* **20** (2), 255–
 918 266.
- 919 COLBURN, DAVID S. & SONETT, CHARLES P. 1966 Discontinuities in the solar wind. *Space Science Reviews* **5**,
 920 439–506.
- 921 COPPI, B., LAVAL, G. & PELLAT, R. 1966 Dynamics of the geomagnetic tail. *Physical Review Letters* **26**,
 922 1207–1210.
- 923 CORONITI, F. V. 1980 On the tearing mode in quasi-neutral sheets. *Journal of Geophysical Research: Space*
 924 *Physics* **85** (A12), 6719–6728.
- 925 CRAMER, NEIL F. 2001 *The Physics of Alfvén Waves*. John Wiley and Sons, Ltd.
- 926 DE KEYSER, J. 2008 Empirical reconstruction. *SSI Scientific Reports Series* **8**, 91–98.
- 927 DENTON, R. E., SONNERUP, B. U. Ö., HASEGAWA, H., PHAN, T. D., RUSSELL, C. T., STRANGWAY, R. J., GILES,
 928 B. L., GERSHMAN, D. & TORBERT, R. B. 2016 Motion of the MMS spacecraft relative to the magnetic
 929 reconnection structure observed on 16 October 2015 at 1307 UT. *Geophysical Research Letters*
 930 **43** (11), 5589–5596.
- 931 DENTON, R. E., SONNERUP, B. U. Ö., RUSSELL, C. T., HASEGAWA, H., PHAN, T.-D., STRANGWAY, R. J., GILES,
 932 B. L., ERGUN, R. E., LINDQVIST, P.-A., TORBERT, R. B., BURCH, J. L. & VINES, S. K. 2018 Determining L
 933 - M - N Current Sheet Coordinates at the Magnetopause From Magnetospheric Multiscale Data.
 934 *Journal of Geophysical Research: Space Physics* **123** (3), 2274–2295.
- 935 DENTON, R. E., TORBERT, R. B., HASEGAWA, H., DORS, I., GENESTRETI, K. J., ARGALL, M. R., GERSHMAN,
 936 D., LE CONTEL, O., BURCH, J. L., RUSSELL, C. T., STRANGWAY, R. J., GILES, B. L. & FISCHER, D.
 937 2020 Polynomial reconstruction of the reconnection magnetic field observed by multiple spacecraft.
 938 *Journal of Geophysical Research: Space Physics* **125** (2), e2019JA027481.
- 939 DORVILLE, NICOLAS, BELMONT, GÉRARD, AUNAI, NICOLAS, DARGENT, JÉRÉMY & REZEAU, LAURENCE 2015a
 940 Asymmetric kinetic equilibria: Generalization of the BAS model for rotating magnetic profile and
 941 non-zero electric field. *Physics of Plasmas* **22** (9), 092904.

- 942 DORVILLE, NICOLAS, BELMONT, GÉRARD, REZEAU, LAURENCE, GRAPPIN, ROLAND & RETINÒ, ALESSANDRO 2014
943 Rotational/compressional nature of the magnetopause: Application of the BV technique on a
944 magnetopause case study. *Journal of Geophysical Research: Space Physics* **119** (3), 1898–1908.
- 945 DORVILLE, NICOLAS, HAALAND, STEIN, ANEKALLU, CHANDRASEKHAR, BELMONT, GÉRARD & REZEAU, LAURENCE
946 2015*b* Magnetopause orientation: Comparison between generic residue analysis and BV method:
947 GRA/BV COMPARISON. *Journal of Geophysical Research: Space Physics* **120** (5), 3366–3379.
- 948 DUNLOP, M.W., SOUTHWOOD, D.J., GLASSMEIER, K.-H. & NEUBAUER, F.M. 1988 Analysis of multipoint
949 magnetometer data. *Advances in Space Research* **8** (9-10), 273–277.
- 950 ERGUN, R. E., TUCKER, S., WESTFALL, J., GOODRICH, K. A., MALASPINA, D. M., SUMMERS, D., WALLACE, J.,
951 KARLSSON, M., MACK, J., BRENNAN, N., PYKE, B., WITHNELL, P., TORBERT, R., MACRI, J., RAU, D., DORS,
952 I., NEEDELL, J., LINDQVIST, P.-A., OLSSON, G. & CULLY, C. M. 2016 The axial double probe and fields
953 signal processing for the MMS mission. *Space Science Reviews* **199** (1), 167–188.
- 954 ESCOUBET, C.P., FEHRINGER, M. & GOLDSTEIN, M.L. 2001 Introduction The Cluster mission. *Annales*
955 *Geophysicae* **19** (10-12).
- 956 ESCOUBET, C.P., SCHMIDT, R. & GOLDSTEIN, M.L. 1997 Cluster -Science and mission overview. *Space Science*
957 *Reviews* **79** (11-32).
- 958 FRISCH, URIEL 1995 *Turbulence: The Legacy of A.N. Kolmogorov*, 1st edn. Cambridge University Press.
- 959 FUSELIER, S. A., TRATTNER, K. J. & PETRINEC, S. M. 2011 Antiparallel and component reconnection
960 at the dayside magnetopause: MULTIPLE MAGNETOPAUSE RECONNECTION. *Journal of*
961 *Geophysical Research: Space Physics* **116** (A10), n/a–n/a.
- 962 GALEEV, A.A. 1979 Reconnection in the magnetotail. *Space Science Reviews* **23** (3).
- 963 GENESTRETI, K. J., NAKAMURA, T. K. M., NAKAMURA, R., DENTON, R. E., TORBERT, R. B., BURCH, J. L.,
964 PLASCHKE, F., FUSELIER, S. A., ERGUN, R. E., GILES, B. L. & RUSSELL, C. T. 2018 How Accurately
965 Can We Measure the Reconnection Rate E_m for the MMS Diffusion Region Event of 11 July
966 2017? *Journal of Geophysical Research: Space Physics* **123** (11), 9130–9149.
- 967 GOSLING, J. T., ASBRIDGE, J. R., BAME, S. J., FELDMAN, W. C., PASCHMANN, G., SCKOPKE, N. & RUSSELL,
968 C. T. 1982 Evidence for quasi-stationary reconnection at the dayside magnetopause. *Journal of*
969 *Geophysical Research: Space Physics* **87** (A4), 2147–2158.
- 970 GUNELL, H., NILSSON, H., STENBERG, G., HAMRIN, M., KARLSSON, T., MAGGIOLO, R., ANDRÉ, M., LUNDIN, R.
971 & DANDOURAS, I. 2012 Plasma penetration of the dayside magnetopause. *Physics of Plasmas* **19** (7),
972 072906.
- 973 HAALAND, S., HASEGAWA, H., PASCHMANN, G., SONNERUP, B. & DUNLOP, M. 2021 20 Years of Cluster
974 Observations: The Magnetopause. *Journal of Geophysical Research: Space Physics* **126** (8),
975 e2021JA029362.
- 976 HAALAND, S., REISTAD, J., TENFJORD, P., GJERLOEV, J., MAES, L., DEKEYSER, J., MAGGIOLO, R., ANEKALLU, C.
977 & DORVILLE, N. 2014 Characteristics of the flank magnetopause: Cluster observations. *Journal of*
978 *Geophysical Research: Space Physics* **119** (11), 9019–9037.
- 979 HAALAND, S. E., SONNERUP, B. U. Ö., DUNLOP, M. W., BALOGH, A., GEORGESCU, E., HASEGAWA, H., KLECKER,
980 B., PASCHMANN, G., PUHL-QUINN, P., RÈME, H., VAITH, H. & VAIVADS, A. 2004 Four-spacecraft
981 determination of magnetopause orientation, motion and thickness: comparison with results from
982 single-spacecraft methods. *Annales Geophysicae* **22** (4), 1347–1365.
- 983 HASEGAWA, AKIRA & UBEROI, CHANCHAL 1982 *The Alfvén wave*. Oak Ridge, TN (USA): U.S. Department of
984 Energy Technical Information Center.
- 985 HASEGAWA, H., SONNERUP, B. U. Ö., KLECKER, B., PASCHMANN, G., DUNLOP, M. W. & RÈME, H. 2005 Optimal
986 reconstruction of magnetopause structures from Cluster data. *Annales Geophysicae* **23** (3), 973–982.
- 987 HAU, L.-N. & SONNERUP, B. U. Ö 1991 Self-consistent gyroviscous fluid model of rotational discontinuities.
988 *Journal of Geophysical Research: Space Physics* **96**, 15767–15778.
- 989 HAU, L.-N. & WANG, B.-J. 2016 Slow shock and rotational discontinuity in MHD and hall MHD models
990 with anisotropic pressure. *Journal of Geophysical Research: Space Physics* **121** (7), 6245–6261.
- 991 HESSE, MICHAEL, AUNAI, NICOLAS, SIBECK, DAVID & BIRN, JOACHIM 2014 On the electron diffusion region in
992 planar, asymmetric, systems. *Geophysical Research Letters* **41** (24), 8673–8680.
- 993 HESSE, MICHAEL, NEUKIRCH, THOMAS, SCHINDLER, KARL, KUZNETSOVA, MASHA & ZENITANI, SEIJI 2011 The
994 Diffusion Region in Collisionless Magnetic Reconnection. *Space Science Reviews* **160** (1-4), 3–23.
- 995 HUDSON, P.D. 1971 Rotational discontinuities in an anisotropic plasma. *Planetary and Space Science*
996 **19** (12), 1693–1699.
- 997 JEFFREY, A. & TANIUTI, T. 1964 *Non-linear Wave Propagation: With Applications to Physics and*
998 *Magnetohydrodynamics (Mathematics in science and engineering ; v. 9)*. Academic Press.

- 999 KING, J. H. & PAPITASHVILI, N. E. 2005 Solar wind spatial scales in and comparisons of hourly Wind and
1000 ACE plasma and magnetic field data. *Journal of Geophysical Research: Space Physics* **110** (A2),
1001 2004JA010649.
- 1002 KIVELSON, M. G. & RUSSELL, C. T., ed. 1995 *Introduction to space physics*. Cambridge University Press,
1003 OCLC: 1124679918.
- 1004 LALLEMENT, R. 2001 Heliopause and astropauses. *Astrophysics and Space Science* **277**, 205–2017.
- 1005 LANDAU, L. D. & LIFSHITZ, E. M. 1987 *Fluid mechanics*. Pergamon Press.
- 1006 LINDQVIST, P.-A., OLSSON, G., TORBERT, R. B., KING, B., GRANOFF, M., RAU, D., NEEDELL, G., TURCO, S.,
1007 DORS, I., BECKMAN, P., MACRI, J., FROST, C., SALWEN, J., ERIKSSON, A., ÅHLÉN, L., KHOTYAINTEV, Y. V.,
1008 PORTER, J., LAPPALAINEN, K., ERGUN, R. E., WERMEER, W. & TUCKER, S. 2016 The spin-plane double
1009 probe electric field instrument for MMS. *Space Science Reviews* **199** (1), 137–165.
- 1010 LIU, YI-HSIN, HESSE, M., CASSAK, P. A., SHAY, M. A., WANG, S. & CHEN, L.-J. 2018 On the collisionless
1011 asymmetric magnetic reconnection rate. *Geophysical Research Letters* **45** (8), 3311–3318.
- 1012 LIU, Y. Y., FU, H. S., CAO, J. B., WANG, Z., HE, R. J., GUO, Z., XU, Y. & YU, Y. 2022 Magnetic discontinuities
1013 in the solar wind and magnetosheath: Magnetospheric multiscale mission (mms) observations. *The*
1014 *Astrophysical Journal* **930**.
- 1015 LUNDIN, R. & DUBININ, E. 1984 Solar wind energy transfer regions inside the dayside magnetopause—I.
1016 Evidence for magnetosheath plasma penetration. *Planetary and Space Science* **32** (6), 745–755.
- 1017 LYNN, Y. M. 1967 Discontinuities in an anisotropic plasma. *Physics of Fluids* **10** (10), 2278.
- 1018 LYU, L. H. & KAN, J. R. 1989 Structures of alfvén shocks: S-shaped magnetic hodogram observed at the
1019 magnetopause. *Geophysical Research Letters* **16** (5), 349–352.
- 1020 McPHERRON, ROBERT L. 1979 Magnetospheric substorms. *Reviews of Geophysics* **17** (4), 657–681.
- 1021 MICHOTTE DE WELLE, B., AUNAI, N., NGUYEN, G., LAVRAUD, B., GÉNOT, V., JEANDET, A. & SMETS, R.
1022 2022 Global Three-Dimensional Draping of Magnetic Field Lines in Earth’s Magnetosheath From
1023 In-Situ Spacecraft Measurements. *Journal of Geophysical Research: Space Physics* **127** (12),
1024 e2022JA030996.
- 1025 NEUBAUER, FRITZ MANFRED 1970 Jump relations for shocks in an anisotropic magnetized plasma. *Zeitschrift*
1026 *für Physik A Hadrons and nuclei* **237** (3), 205–223.
- 1027 NEUGEBAUER, M. 2006 Comment on the abundances of rotational and tangential discontinuities in the solar
1028 wind. *Journal of Geophysical Research: Space Physics* **111** (A4), 2005JA011497.
- 1029 NEUGEBAUER, MARCIA, GIACALONE, JOE, MAKSIMOVIC, M., ISSAUTIER, K., MEYER-VERNET, N., MONCUQUET, M.
1030 & PANTELLINI, F. 2010 Progress in the Study of Interplanetary Discontinuities. In *AIP Conference*
1031 *Proceedings*, pp. 194–197. Saint-Malo, (France).
- 1032 NGUYEN, G., AUNAI, N., MICHOTTE DE WELLE, B., JEANDET, A., LAVRAUD, B. & FONTAINE, D. 2022 Massive
1033 Multi-Mission Statistical Study and Analytical Modeling of the Earth’s Magnetopause: 1. A Gradient
1034 Boosting Based Automatic Detection of Near-Earth Regions. *Journal of Geophysical Research:*
1035 *Space Physics* **127** (1), e2021JA029773.
- 1036 OTTO, ANTONIUS 2005 *The Magnetosphere*, pp. 133–192. Berlin, Heidelberg: Springer Berlin Heidelberg.
- 1037 PANOV, E. V., ARTEMYEV, A. V., NAKAMURA, R. & BAUMJOHANN, W. 2011 Two types of tangential
1038 magnetopause current sheets: Cluster observations and theory: TANGENTIAL MAGNETOPAUSE
1039 STRUCTURE. *Journal of Geophysical Research: Space Physics* **116** (A12), n/a–n/a.
- 1040 PARKS, GEORGE K. 2019 *Physics of space plasmas: an introduction*. "The Advanced book program." .
1041 Routledge, Taylor & Francis Group.
- 1042 PASCHMANN, GÖTZ 1984 Plasma and particle observations at the magnetopause: Implications for
1043 reconnection. In *Geophysical Monograph Series* (ed. Edward W. Hones), , vol. 30, pp. 114–123.
1044 Washington, D. C.: American Geophysical Union.
- 1045 PASCHMANN, G., HAALAND, S., SONNERUP, B. & KNETTER, T. 2013 Discontinuities and Alfvénic fluctuations in
1046 the solar wind. *Annales Geophysicae* **31** (5), 871–887.
- 1047 PASCHMANN, G., HAALAND, S. E., PHAN, T. D., SONNERUP, B. U. Ö., BURCH, J. L., TORBERT, R. B., GERSHMAN,
1048 D. J., DORELLI, J. C., GILES, B. L., POLLOCK, C., SAITO, Y., LAVRAUD, B., RUSSELL, C. T., STRANGEWAY,
1049 R. J., BAUMJOHANN, W. & FUSELIER, S. A. 2018a Large-Scale Survey of the Structure of the Dayside
1050 Magnetopause by MMS. *Journal of Geophysical Research: Space Physics* **123** (3), 2018–2033.
- 1051 PASCHMANN, G., HAALAND, S. E., PHAN, T. D., SONNERUP, B. U. Ö., BURCH, J. L., TORBERT, R. B., GERSHMAN,
1052 D. J., DORELLI, J. C., GILES, B. L., POLLOCK, C., SAITO, Y., LAVRAUD, B., RUSSELL, C. T., STRANGEWAY,
1053 R. J., BAUMJOHANN, W. & FUSELIER, S. A. 2018b Large-Scale Survey of the Structure of the Dayside
1054 Magnetopause by MMS. *Journal of Geophysical Research: Space Physics* **123** (3), 2018–2033.

- 1055 PASSOT, T. & SULEM, P. L. 2006 A fluid model with finite Larmor radius effects for mirror mode dynamics.
1056 *Journal of Geophysical Research: Space Physics* **111** (A4), 2005JA011425.
- 1057 PHAN, T. D., KISTLER, L. M., KLECKER, B., HAERENDEL, G., PASCHMANN, G., SONNERUP, B. U. Ö., BAUMJOHANN,
1058 W., BAVASSANO-CATTANEO, M. B., CARLSON, C. W., DiLELLIS, A. M., FORNACON, K.-H., FRANK, L. A.,
1059 FUJIMOTO, M., GEORGESCU, E., KOKUBUN, S., MOEBIUS, E., MUKAI, T., ØIEROSET, M., PATERSON, W. R.
1060 & REME, H. 2000 Extended magnetic reconnection at the Earth's magnetopause from detection of
1061 bi-directional jets. *Nature* **404** (6780), 848–850.
- 1062 PHAN, T. D., SHAY, M. A., GOSLING, J. T., FUJIMOTO, M., DRAKE, J. F., PASCHMANN, G., ØIEROSET, M.,
1063 EASTWOOD, J. P. & ANGELOPOULOS, V. 2013 Electron bulk heating in magnetic reconnection at Earth's
1064 magnetopause: Dependence on the inflow Alfvén speed and magnetic shear. *Geophysical Research*
1065 *Letters* **40** (17), 4475–4480.
- 1066 POLLOCK, C., MOORE, T., JACQUES, A., BURCH, J., GLIESE, U., SAITO, Y., OMOTO, T., AVANOV, L., BARRIE, A.,
1067 COFFEY, V., DORELLI, J., GERSHMAN, D., GILES, B., ROSNACK, T., SALO, C., YOKOTA, S., ADRIAN, M.,
1068 Aoustin, C., AULETTI, C., AUNG, S., BIGIO, V., CAO, N., CHANDLER, M., CHORNAY, D., CHRISTIAN, K.,
1069 CLARK, G., COLLINSON, G., CORRIS, T., DE LOS SANTOS, A., DEVLIN, R., DIAZ, T., DICKERSON, T.,
1070 DICKSON, C., DIEKMANN, A., DIGGS, F., DUNCAN, C., FIGUEROA-VINAS, A., FIRMAN, C., FREEMAN, M.,
1071 GALASSI, N., GARCIA, K., GOODHART, G., GUERRERO, D., HAGEMAN, J., HANLEY, J., HEMMINGER, E.,
1072 HOLLAND, M., HUTCHINS, M., JAMES, T., JONES, W., KREISLER, S., KUJAWSKI, J., LAVU, V., LOBELL, J.,
1073 LeCOMTE, E., LUKEMIRE, A., MacDONALD, E., MARIANO, A., MUKAI, T., NARAYANAN, K., NGUYAN, Q.,
1074 ONIZUKA, M., PATERSON, W., PERSYN, S., PIEPGRASS, B., CHENEY, F., RAGER, A., RAGHURAM, T., RAMIL,
1075 A., REICHTHAL, L., RODRIGUEZ, H., ROUZAUD, J., RUCKER, A., SAITO, Y., SAMARA, M., SAUVAUD, J.-A.,
1076 SCHUSTER, D., SHAPIRIO, M., SHELTON, K., SHER, D., SMITH, D., SMITH, K., SMITH, S., STEINFELD, D.,
1077 SZYMKIEWICZ, R., TANIMOTO, K., TAYLOR, J., TUCKER, C., TULL, K., UHL, A., VLOET, J., WALPOLE, P.,
1078 WEIDNER, S., WHITE, D., WINKERT, G., YEH, P.-S. & ZEUCH, M. 2016 Fast plasma investigation for
1079 magnetospheric multiscale. *Space Science Reviews* **199** (1), 331–406.
- 1080 REZEAU, L., BELMONT, GERARD, MANUZZO, ROBERTO, AUNAI, NICOLAS & DARGENT, J. 2018 Analyzing the
1081 magnetopause internal structure: New possibilities offered by mms tested in a case study. *Journal of*
1082 *Geophysical Research: Space Physics* **123**.
- 1083 RICHARDSON, J. D., BURLAGA, L. F., ELLIOTT, H., KURTH, W. S., LIU, Y. D. & VON STEIGER, R. 2022 Observations
1084 of the outer heliosphere, heliosheath, and interstellar medium. *Space Science Reviews* **218** (4), 35.
- 1085 RUSSELL, C. T., ANDERSON, B. J., BAUMJOHANN, W., BROMUND, K. R., DEARBORN, D., FISCHER, D., LE, G.,
1086 LEINWEBER, H. K., LENEMAN, D., MAGNES, W., MEANS, J. D., MOLDWIN, M. B., NAKAMURA, R., PIERCE,
1087 D., PLASCHKE, F., ROWE, K. M., SLAVIN, J. A., STRANGWAY, R. J., TORBERT, R., HAGEN, C., JERNEJ, I.,
1088 VALAVANOGLU, A. & RICHTER, I. 2016 The magnetospheric multiscale magnetometers. *Space Science*
1089 *Reviews* **199** (1), 189–256.
- 1090 SHI, Q. Q., SHEN, C., PU, Z. Y., DUNLOP, M. W., ZONG, Q.-G., ZHANG, H., XIAO, C. J., LIU, Z. X. &
1091 BALOGH, A. 2005 Dimensional analysis of observed structures using multipoint magnetic field
1092 measurements: Application to cluster: STRUCTURE DIMENSIONALITY DETERMINATION.
1093 *Geophysical Research Letters* **32** (12), n/a–n/a.
- 1094 SHI, Q. Q., TIAN, A. M., BAI, S. C., HASEGAWA, H., DEGELING, A. W., PU, Z. Y., DUNLOP, M., GUO, R. L., YAO,
1095 S. T., ZONG, Q.-G., WEI, Y., ZHOU, X.-Z., FU, S. Y. & LIU, Z. Q. 2019 Dimensionality, Coordinate
1096 System and Reference Frame for Analysis of In-Situ Space Plasma and Field Data. *Space Science*
1097 *Reviews* **215** (4), 35.
- 1098 SHUE, J.-H., CHAO, J. K., FU, H. C., RUSSELL, C. T., SONG, P., KHURANA, K. K. & SINGER, H. J. 1997 A
1099 new functional form to study the solar wind control of the magnetopause size and shape. *Journal of*
1100 *Geophysical Research: Space Physics* **102** (A5), 9497–9511.
- 1101 SMITH, EDWARD J. 1973 Identification of interplanetary tangential and rotational discontinuities. *Journal of*
1102 *Geophysical Research* **78** (13), 2054–2063.
- 1103 SONNERUP, B. & SCHEIBLE, M. 1998 Minimum and maximum variance analysis. In *Analysis Methods for*
1104 *Multi- Spacecraft Data*, pp. pp. 185–220. Int. Space Sci. Inst./Eur. Space Agency, Bern/Paris.
- 1105 SONNERUP, B. U. O. & LEDLEY, B. G. 1974 Magnetopause rotational forms. *Journal of Geophysical Research*
1106 **79** (28), 4309–4314.
- 1107 SONNERUP, B. U. Ö & CAHILL, L. J. 1967 Magnetopause structure and attitude from Explorer 12 observations.
1108 *Journal of Geophysical Research* **72** (1), 171.
- 1109 SONNERUP, B. U. Ö., HAALAND, S., PASCHMANN, G., DUNLOP, M. W., RÈME, H. & BALOGH, A. 2006 Orientation
1110 and motion of a plasma discontinuity from single-spacecraft measurements: Generic residue analysis
1111 of Cluster data. *Journal of Geophysical Research: Space Physics* **111** (A5), 2005JA011538.

- 1112 STASIEWICZ, KRZYSZTOF 1989 A fluid finite ion larmor radius model of the magnetopause layer. *Journal of*
1113 *Geophysical Research* **94**, 8827–8834.
- 1114 STASIEWICZ, K. 1993 Finite larmor radius effects in the magnetosphere. *Space Science Reviews* **65** (3), 221–
1115 252.
- 1116 SWISDAK, M., ROGERS, B. N., DRAKE, J. F. & SHAY, M. A. 2003 Diamagnetic suppression of component
1117 magnetic reconnection at the magnetopause. *Journal of Geophysical Research: Space Physics*
1118 **108** (A5), 2002JA009726.
- 1119 TORBERT, R. B., BURCH, J. L., GILES, B. L., GERSHMAN, D., POLLOCK, C. J., DORELLI, J., AVANOV, L., ARGALL,
1120 M. R., SHUSTER, J., STRANGWAY, R. J., RUSSELL, C. T., ERGUN, R. E., WILDER, F. D., GOODRICH, K.,
1121 FAITH, H. A., FARRUGIA, C. J., LINDQVIST, P.-A., PHAN, T., KHOTYAINTEV, Y., MOORE, T. E., MARKLUND,
1122 G., DAUGHTON, W., MAGNES, W., KLETZING, C. A. & BOUNDS, S. 2016 Estimates of terms in Ohm's
1123 law during an encounter with an electron diffusion region. *Geophysical Research Letters* **43** (12),
1124 5918–5925.
- 1125 TRATTNER, K. J., PETRINEC, S. M. & FUSELIER, S. A. 2021 The Location of Magnetic Reconnection at Earth's
1126 Magnetopause. *Space Science Reviews* **217** (3), 41.
- 1127 TSURUTANI, B.T., ZHOU, X.-Y., VASYLIUNAS, V.M., HAERENDEL, G., ARBALLO, J.K. & LAKHINA, G.S. 2001
1128 Interplanetary Shocks, Magnetopause Boundary Layers and Dayside Auroras: The Importance of
1129 a Very Small Magnetospheric Region. *Surveys in Geophysics* **22** (2), 101–130.
- 1130 TSURUTANI, BRUCE T. & SMITH, EDWARD J. 1979 Interplanetary discontinuities: Temporal variations and the
1131 radial gradient from 1 to 8.5 AU. *Journal of Geophysical Research: Space Physics* **84** (A6), 2773–
1132 2787.
- 1133 VINES, S. K., FUSELIER, S. A., TRATTNER, K. J., PETRINEC, S. M. & DRAKE, J. F. 2015 Ion acceleration
1134 dependence on magnetic shear angle in dayside magnetopause reconnection. *Journal of Geophysical*
1135 *Research: Space Physics* **120** (9), 7255–7269.
- 1136 ŠAFRÁNKOVÁ, J., NĚMEČEK, Z., DUŠÍK, Š., PŘECH, L., SIBECK, D. G. & BORODKOVA, N. N. 2002 The
1137 magnetopause shape and location: a comparison of the Interball and Geotail observations with
1138 models. *Annales Geophysicae* **20** (3), 301–309.